Numerical Simulation of Surface Patterns on Sublimating Ablative Materials

A THESIS
SUBMITTED TO THE FACULTY OF THE GRADUATE SCHOOL
OF THE UNIVERSITY OF MINNESOTA
BY

Loretta Treviño

IN PARTIAL FULFILLMENT OF THE REQUIREMENTS
FOR THE DEGREE OF
Doctor of Philosophy

Graham V. Candler, Advisor

May, 2021

Acknowledgements

Thank you to my advisor Prof. Graham Candler for suggesting a challenging topic and never giving up on me. Thank you to Dr. Vladimyr Gidzak for allowing me to use his ablation code as part of the learning process and Dr. Ioannis Nompelis for always being a mentor. Thank you to Dr. Sidharth GS for endless crosshatching discussions and for being one of my biggest supporters through graduate school. Thank you to my employer and co-workers at Stratolaunch for allowing me to have a flexible schedule while writing my thesis, and to Mr. Kelton Busby for cheering me across the finish line this past year.

Dedication

For my colleagues who are a constant source of encouragement and support.

Abstract

Thermal protection systems made of ablative materials are a well-known solution to protect vehicles from high heating environments. As the material changes shape due to the ablation process, several patterns may develop. One pattern that develops is a very regularly ordered diamond-shaped pattern known as crosshatching. The mechanism for which initiates the pattern development is not yet known. This research aims to study the ablation process and its contribution to crosshatching by implementing and validating a camphor sublimating boundary condition into the US3D fluid-solid solver. This work shows that the sublimation process can develop localized deep grooves, leading to the onset of crosshatching. The stability of a sublimating boundary layer is also not well studied. Through this work, it was demonstrated that the presence of camphor in the boundary layer is stabilizing. There are still many open questions on how the camphor presence affects a boundary layer's stability and how it could potentially play a role in the initiation of crosshatching.

Contents

List of Tables

List of Figures

Chapter 1

Introduction

A vehicle that enters into a planetary atmosphere requires a thermal protection system (TPS) to protect it from overheating. A common TPS used is an ablative material that undergoes the sublimation chemical process. A subliming ablator protects a vehicle from overheating by acting as a heat sink until the surface reaches its sublimation temperature; once the materials start to sublimate, it removes heat from the surface. A consequence of the sublimation process, however, is shape change and potential surface pattern development. Ablation surfaces have exhibited different surface patterns in both flight and ground experiments, including streamwise grooves, pits, ablation wedges, scallops, and crosshatching.

Figure 1.1 shows images from a wind tunnel campaign performed by Stock illustrating three common ablation patterns [8]. The first pattern on the left is streamwise grooves which are etched into the surface by streamwise vortices that increase heat and mass transfer rates[20, 9, 21]. Mechanisms that generate streamwise vortices include surface irregularities, backward-facing steps, and concave surfaces. The second image is of turbulent wedges created due to turbulent heating. A local roughness element can trip the laminar boundary layer, causing lateral turbulence, which increases local heating rates and generates ablation wedges. Crosshatching is the final pattern and is made of very regular diamond shapes. The mechanism for the initiation of the crosshatching pattern is unknown.

The crosshatching patterns develop on both experiments and recovered vehicles and can occur on all types of materials. They form on melting, charing, and subliming

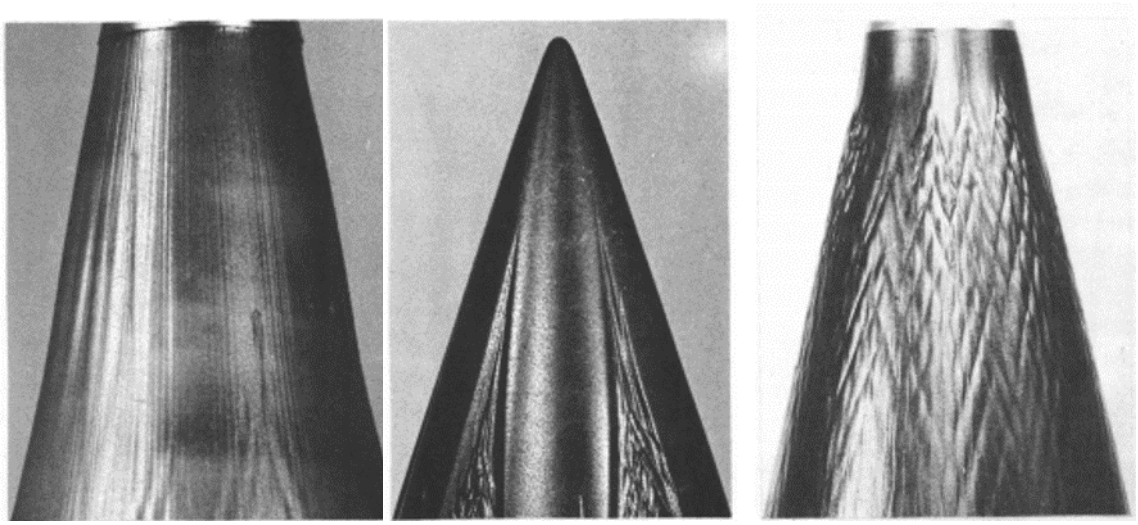

(a) Streamwise Grooves (b) Ablation Wedges (c) Crosshatching

Figure 1.1: Ablation Surface Patterns [8]

materials such as phenolics, glass, plastics, and even wood. Despite the ablation process, which is very different for all these materials, the crosshatching patterns are persistent in their formation. Figure 1.2 illustrates vastly different material types and testing environments where crosshatching patterns formed, and Table 1.1 is a summary by Stock where crosshatching has been observed [1].

Flight conditions in low and high enthalpy environments, various ablation modes and materials, and even different model configurations developed the diamond patterns. Although the model and test environments are very different, the patterns do have some commonality and are correlated to boundary layer properties. Figure 1.3 is a plot of the cant angle versus the edge Mach number for various materials at different facilities. The angle of the diamond pattern is related to the edge Mach number and shows a similar trend for all materials and test facilities. Similarly, the pattern wavelength is correlated to the edge pressure shown in Figure 1.4.

Crosshatching patterns eventually degenerate to scallop patterns. Figure 1.5 is an example of experiments of Grabow and White that show this progression[11]. The scallop patterns are also found on natural objects such as meteorites. Scallops on meteorites are called regmaglypts which are shallow depressions on the surface that

Table 1.1: Summary of Crosshatching Observations In the Literature [1]

Flight conditions	• High enthalpy environment – Re-entry vehicles [20, 24] – Ballistic range models [22, 25] • Low enthalpy environment – Wind-Tunnel models [20, 24, 21, 25, 12, 26, 27, 15, 28, 18]
Ablation modes	• Melting [24, 21, 25, 22, 15] • Melting and vaporizing [25] • Subliming [24, 21, 12, 26, 27, 15, 28, 18] • Charforming [24]
Materials	• Acrylics [20, 24, 25, 22, 25] • Phenolics [24, 24, 27, 28, 18] • Teflon [24, 27, 28, 18] • Camphor [21, 12, 26] [15] • Wood [24] • Wax [15]
Configurations	• Two-dimensional models [20, 24] • Asymmetric models [20, 24, 21, **?**, 22, 12, 26, 15, 28, 18] • Inside circular tubes [27]

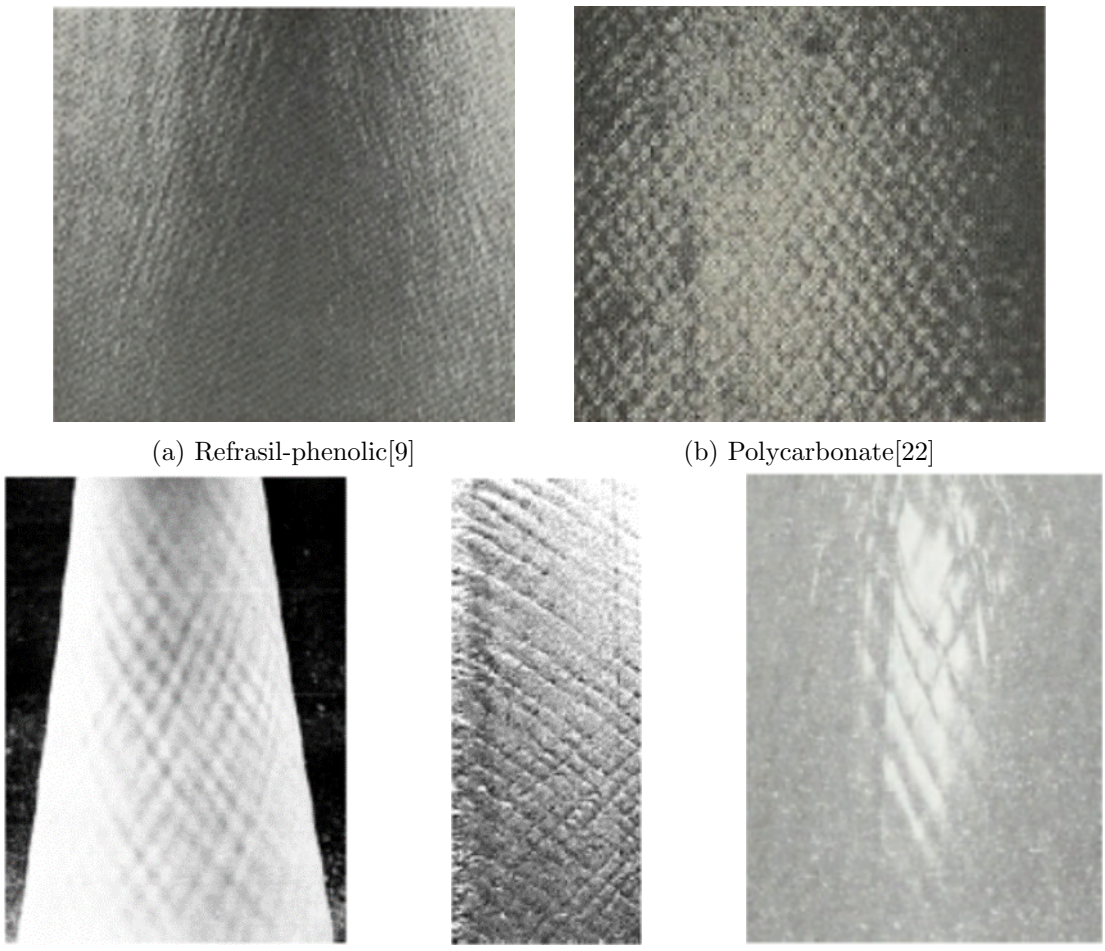

(a) Refrasil-phenolic[9] (b) Polycarbonate[22]

(c) PTFE[20] (d) Pine[9] (e) Camphor [23]

Figure 1.2: Crosshatching on Different Materials

are believed to be formed by local ablation of material from the surface as the meteor passes through the Earth's atmosphere. Figure 1.6 are images of meteorites that exhibit regmaglypts. If the meteorite maintains a fixed orientation, it develops a conical nose similar to the Karakol Russian 1840 meteorite. As the object is changing shape, its body dynamics are changing, and it is of practical interest to understand how this affects controllability. The shape change also creates localized heating that is undesirable for vehicles designed for a specific predicted heat load.

McDevitt at NASA Ames studied the effect of body dynamics on ammonium chloride and camphor cones with a steel nose spike[12]. A gas-bearing apparatus allowed the test

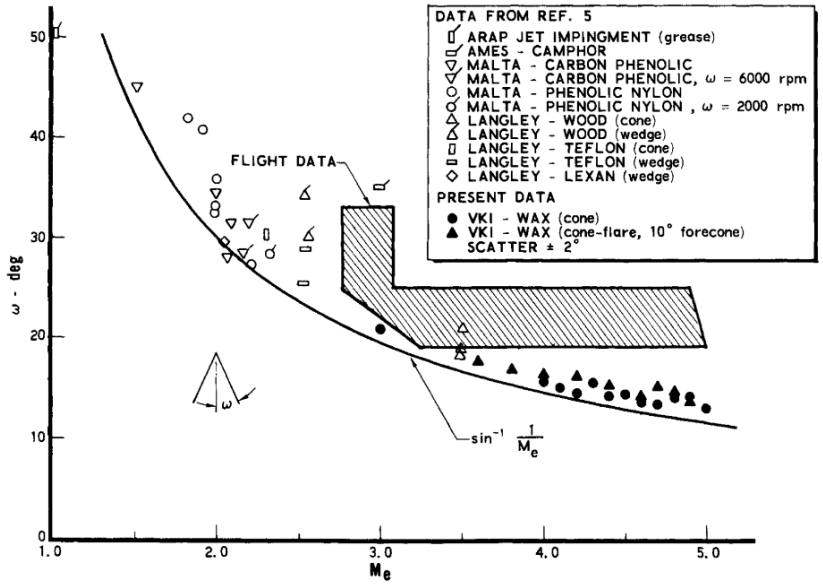

Figure 1.3: Influence of the local Mach Number M_e on the cant angle ω [9]

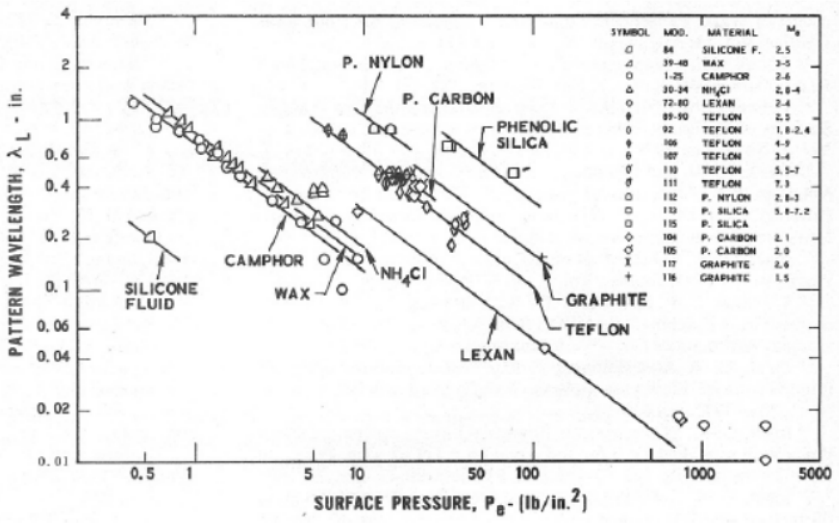

Figure 1.4: Pattern wavelength-surface pressure correlation based on work of White and Grabow [10] [11]

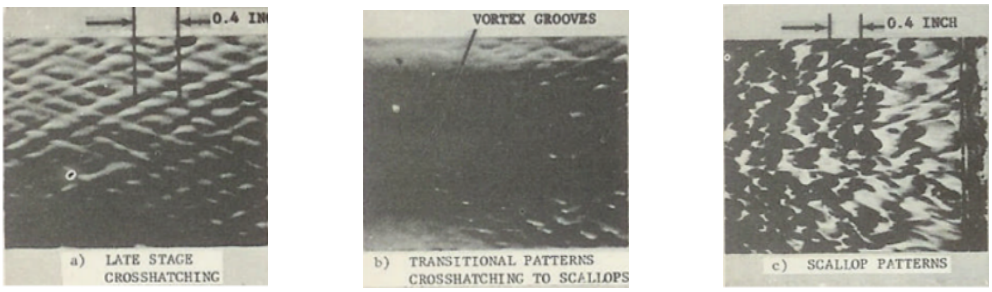

(a) Crosshatching (b) Transitional (c) Scallops

Figure 1.5: Scallops Example in Grabow and White Experiments [11]

(a) Karakol Russia, 1840 (b) Cabin Creek Arkansas, 1886

Figure 1.6: Example Meteorites

models to be free in roll to obtain roll characteristics. In his experiments, the ablation patterns he observed were streamwise grooves, turbulent wedges, and crosshatching. Figure 1.7 is an example of his results. He observed longitudinal striations almost immediately, but the crosshatching patterns only occurred after 20 seconds. There is an initial roll due to a slight mass asymmetry resulting from the insertion process, but then there is a rapid increase in roll shortly after the appearance of crosshatching.

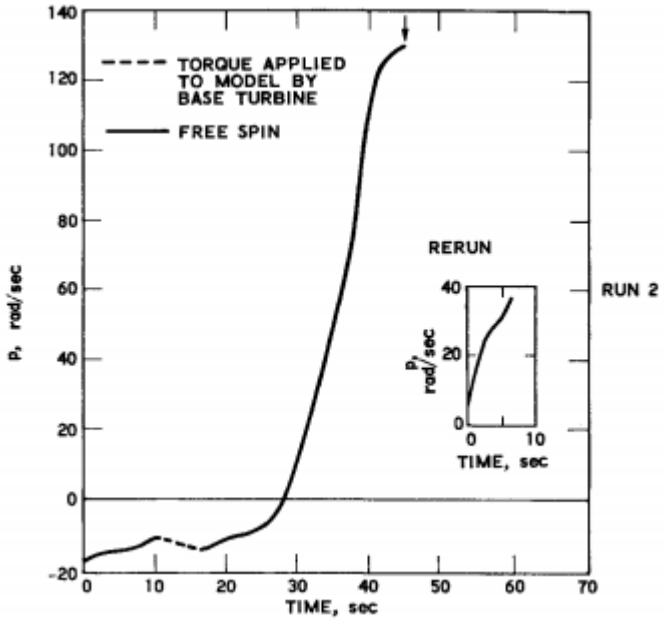

Figure 1.7: Roll behavior of ablating 30^0 NH_4Cl cones at α=0^0; from McDevitt. [12]

1.1 Scope of Current Work

It is desirable to understand the crosshatching phenomenon to avoid undesirable outcomes such as loss of vehicle or under-designed thermal protection systems. There is still no one agreed-upon initiating mechanism through the extensive experimental and theoretical studies conducted in the literature. There are a few characteristics that were common throughout the literature for the presence of crosshatching on all types of ablation materials:

1. Supersonic boundary layer is required
2. Patterns happen in transitional or turbulent flow
3. Pattern shapes are highly correlated with boundary layer edge properties
4. A very thin boundary layer is required

Prior understanding of the crosshatching phenomena was primarily focused on experimental and theoretical work, and the bulk of the research was conducted fifty years

ago before advanced computational methods. Since the early 1970s, only a handful of experiments by Qun [16] and Turchi at VKI are available in the literature. No numerical simulations have studied this phenomenon using Computational Fluid Dynamics (CFD). The scope of this work is to implement a camphor low-temperature ablation boundary condition into a CFD solver to study the conditions for which crosshatching was observed and investigate possible initiation mechanisms for this fluid dynamics mystery.

Chapter 2

Postulated Mechanisms

Many attempts to determine the physical mechanism that initiate crosshatching was studied experimentally and theoretically. The majority of the published work is from the late 1960s early 1970s, and since then, very few researchers have studied crosshatching. Several postulated mechanisms in the literature include vortex initiation, groove marching process, vortex turbulent wedge interaction, surface deformation instabilities, and liquid layer instabilities. Not one of these postulated mechanisms has yet to explain the formation of the crosshatching patterns fully. An excellent review by Swigart provides further detail of many postulates[29]. This chapter will briefly review the key proposed mechanisms known to date.

2.1 Vortex Mechanism

Some of the earliest observations of crosshatched patterns by Canning showed experimental evidence of streamwise vortices upstream and in the vicinity of the crosshatching patterns, which sparked a possible relationship between the patterns formation and streamwise vortices [22]. Tobak presented a correlation using the results of linearized wing theory illustrated in Figure 2.1[13]. He showed that equally spaced streamwise vortices in the presence of Mach cones could produce streamwise and spanwise periodic pressure distributions. When the ablation process begins, the surface with higher pressure will start to recess rapidly, thus creating a pit that will become the apex of the Mach cone. Once the Mach cone starts to interact with the vortices, a crosshatching

pattern of pressure fluctuations will form.

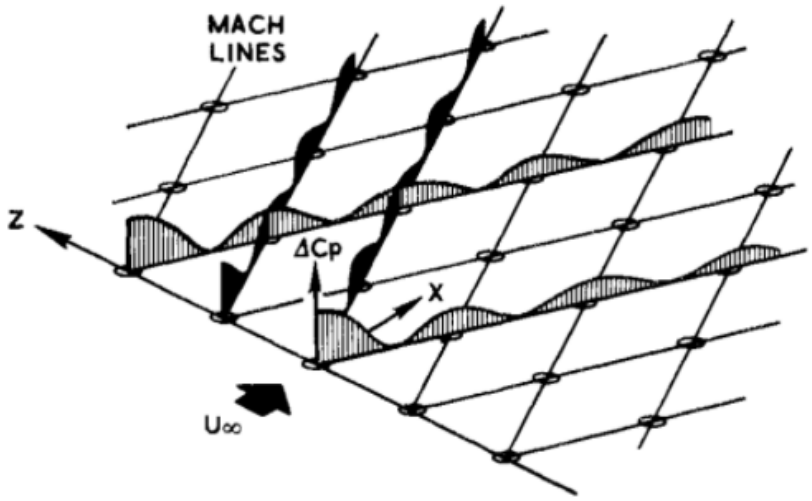

Figure 2.1: Perturbation Pressure Distribution Resulting From Analysis of Tobak [13]

2.2 Groove Marching Process Mechanism

A possible mechanism postulated by Mirels considers a shock marching process[14]. He proposed that the initiation begins with a surface roughness generating a weak conical shock. The shock then locally overpressurizes the surface, causing a locally higher ablation rate, resulting in a groove. This nonlinear interaction causes an increase in the local wave strength and ablation rate. The localized increased blowing due to the increased ablation sets up another shock, and the process repeats itself. The result is a series of roughly equally spaced grooves formed by a downstream shock marching process. Several experimental pieces of evidence support this hypothesis including, the requirement for supersonic flow, an ablative surface is required to enhance the local shock strength, and the surface pressure must be above a critical value to ensure sufficient heat transfer to provide effective ablation rates. Figure 2.2 represents the shock marching process proposed by Mirels [28].

Figure 2.3 is a Stock experiment of a wax cone with a steel tip. It illustrates the groove marching process through a time history of pattern development proposed by

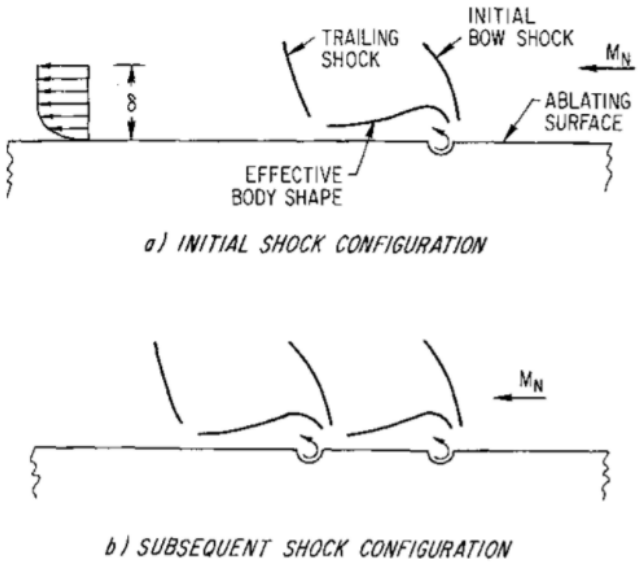

Figure 2.2: Representation of shock marching process [14]

Mirels. Initially, the patterns form just downstream of the wax-steel junction, and as time progresses, the patterns propagate and march downstream. The patterns eventually form scallops similar to the regmaglypts patterns on meteorites and the experiments by Grabow and White.

2.3 Liquid Layer Mechanism

The stability of a thin liquid layer was studied by Nachtsheim and Hagen experimentally as a mechanism for the development of crosshatching[30]. The main objective of this experiment was to determine if the pattern formation required ablation. The experimental campaign was conducted at the NASA Ames Continuous Flow Supersonic Wind Tunnel at Mach 2.8 on a 10^o half-angle conical model made of Plexiglas with slots at the tip. A liquid with a low vapor pressure poured onto the model surface through at the tip with a wide range of viscosity. The higher viscosity liquids were desirable for their low vapor pressure, which was negligible up to 200^oC. The results in Figure 2.4a photograph show that crosshatching patterns in liquid films can form without ablation.

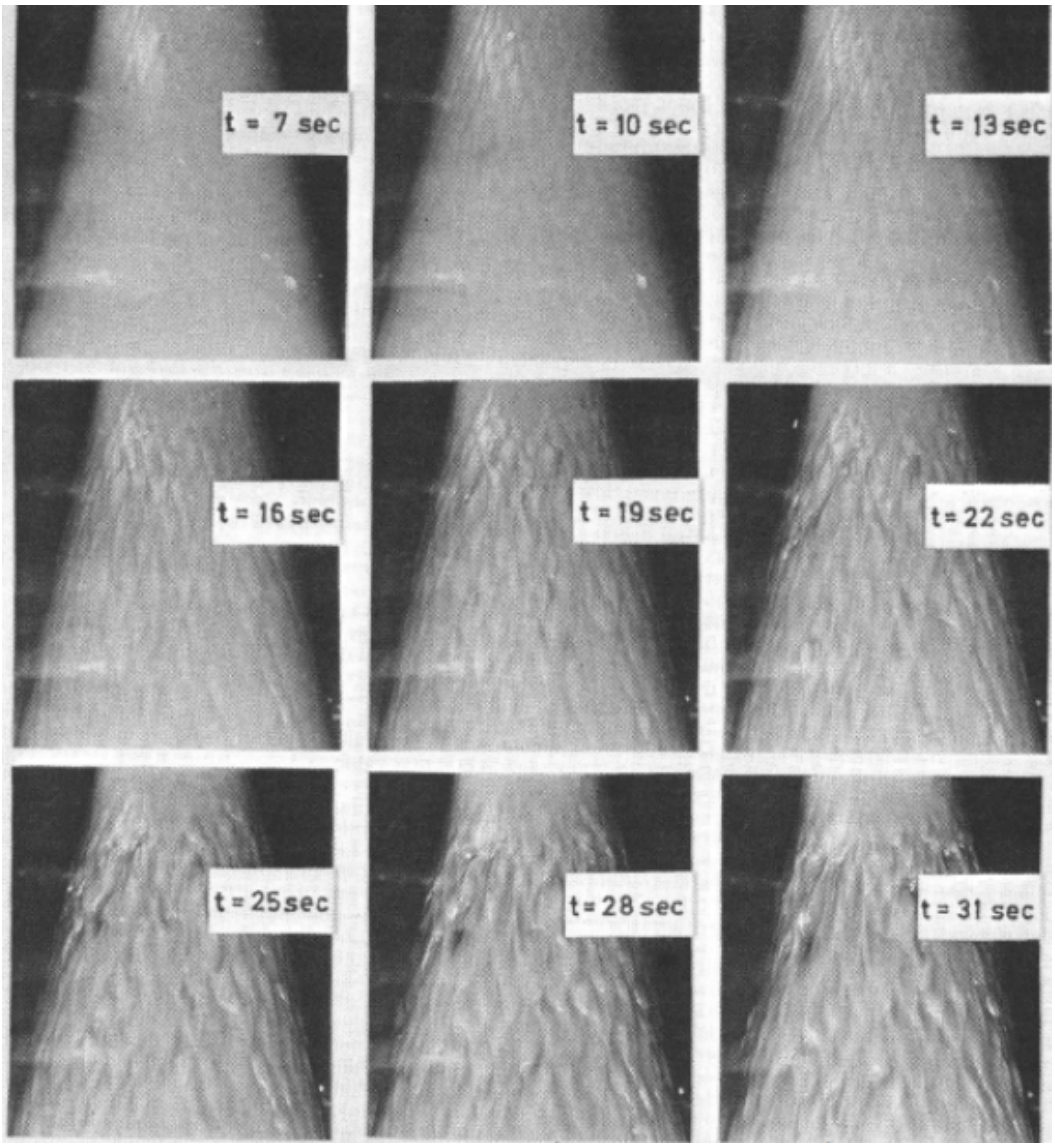

Figure 2.3: Stock Wax-Steel Cone Experiment Time Evolution of Pattern Development [15]

The patterns formed were then compared with observations made with linear stability theory. For the test conditions and patterns shown in Figure 2.4a are compared with the predictions of linear stability analysis in Figure 2.4b. The horizontal axis is a modified friction coefficient, and the vertical axis is a dimensionless wave number. According to Nachtsheim's linear stability analysis, amplified waves are to the right of the curve, and the damped waves are to the left of the neutral stability curve for a fixed Weber number. The observed patterns in Nachtsheim's experiments are in the unstable amplification region shown in Figure 2.4b.

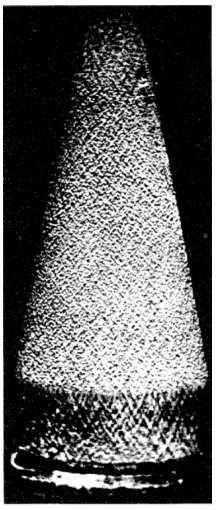

(a) Crosshatched patterns on conical model[30]

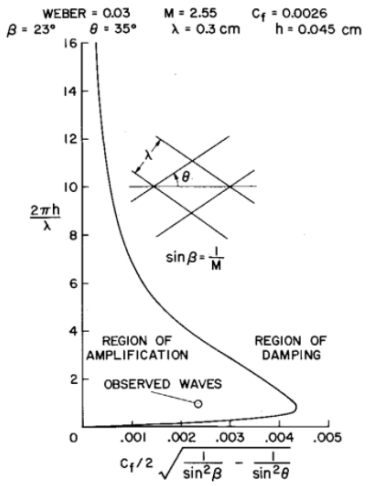

(b) Linear Stability Analysis[18]

Figure 2.4: Nachtsheim Liquid Layer Stability Analysis

Nachtsheim and Larson also studied Teflon cones in a hydrogen-oxygen rocket motor test facility[18]. The objective of this study was to determine if the surface melt Reynolds number influences the formation of crosshatching. The test article studied was a Teflon cone filled with different percentages of graphite and glass. They discovered that as the percentage of glass in the model increases, increasing the viscosity of the melt layer and the liquid Reynolds number resulted in the pattern formation suppression. Figure 2.5b is a photograph of the glass-filled Teflon cones and from left to right, increasing the percentage of glass-filled Teflon. The patterns are shown at the lower liquid Reynolds number condition, while the highest Re_L crosshatching is not visible.

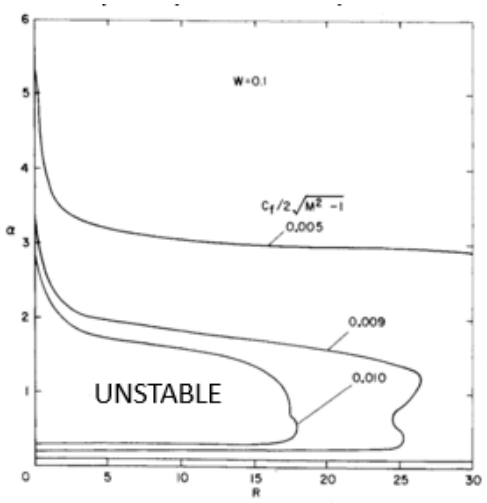

(a) Neutral stability curve [31]

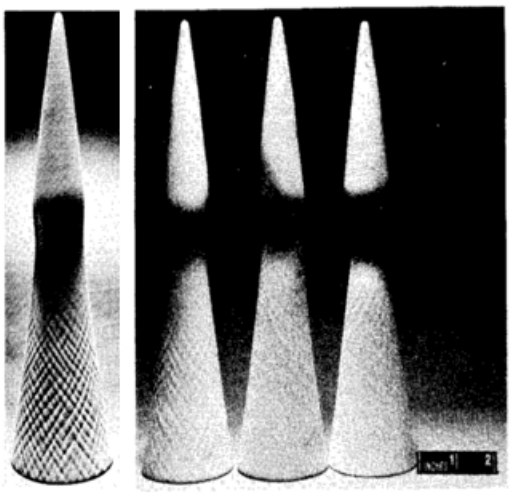

(b) Glass-filled TFE 7%, 15%, 20% and 25% from left to right [18]

Figure 2.5: Nachtsheim stability analysis and experimental cones

This experimental outcome is also consistent with the linear stability analysis performed by Nachtsheim [31].

2.4 Vortex Turbulent Wedges Interaction Mechanism

One of the most recent crosshatching studies conducted by Qun tested a sphere-cone model made of wax at various Mach numbers and stagnation pressures. The primary objective of the study was to understand how freestream conditions affect ablation pattern formation. In the experiments for a given Mach number and stagnation temperature, the total pressure was increased. Figure 2.6 is a plot of the different ablation patterns observed during the experiments. The patterns observed include fine striations, smooth surface, narrow grooves, pits, ablation wedges, crosshatching, and regmaglypts. It is interesting to note that the same patterns lie with the same iso-Reynolds number lines of the boundary layer. The experiments suggest that the type of pattern formed is related to the Reynolds number of the boundary layer. The appearance of the crosshatching pattern only occurs at a Reynolds number above some critical value.

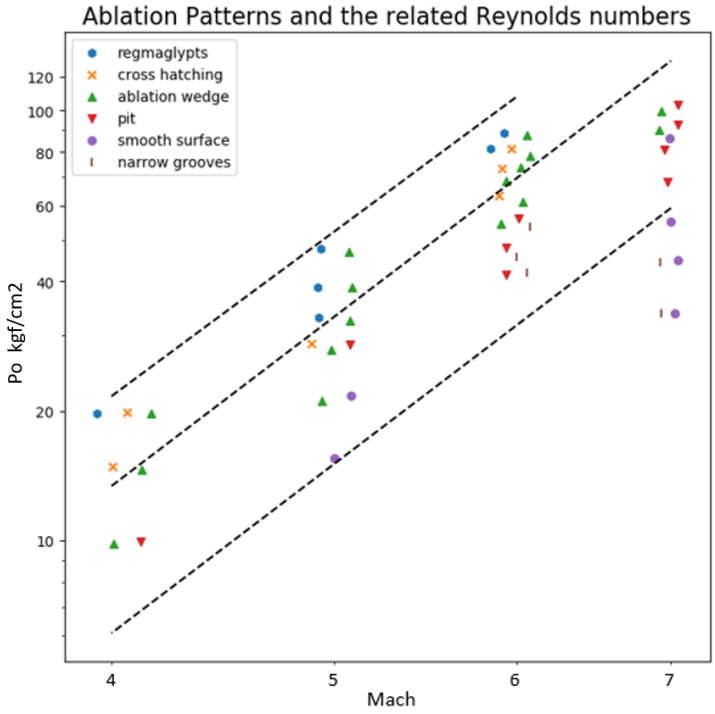

Figure 2.6: Ablation patterns and the related iso-Reynolds number lines plotted with dashed lines for a R_n=25mm sphere cone $T_0 = 130^0$C. [16]

The experimentalist observed that the crosshatching patterns occur after the formation of turbulent wedges and began at the intersection of the turbulent wedges. From their results, they postulated a physical mechanism for the triggering and propagation of crosshatching illustrated in Figure 2.7 and restated as follows[16]:

1. Introduction of a conical shock wave in the supersonic flow outside the boundary layer.

2. The conical shock generated impinges on the boundary layer creating a sharp pressure rise increasing the ablation rate.

3. Increased ablation rate reduces the near-wall friction, forcing the melt layer to flow backward in the local region.

4. Backward flow and the external downstream flow form a new pair of vortices along the intersection line of the shock and the boundary layer.

5. The vortices and the sharp pressure rise produce higher ablation in the local region and from the leading edge of the crosshatching pattern.

6. A vortex along the leading edge of the crosshatching grows and introduces new disturbances in the flow, causing a new conical shock wave.

7. The second row of leading edges of crosshatching is then formed that make the trailing edge of the pattern.

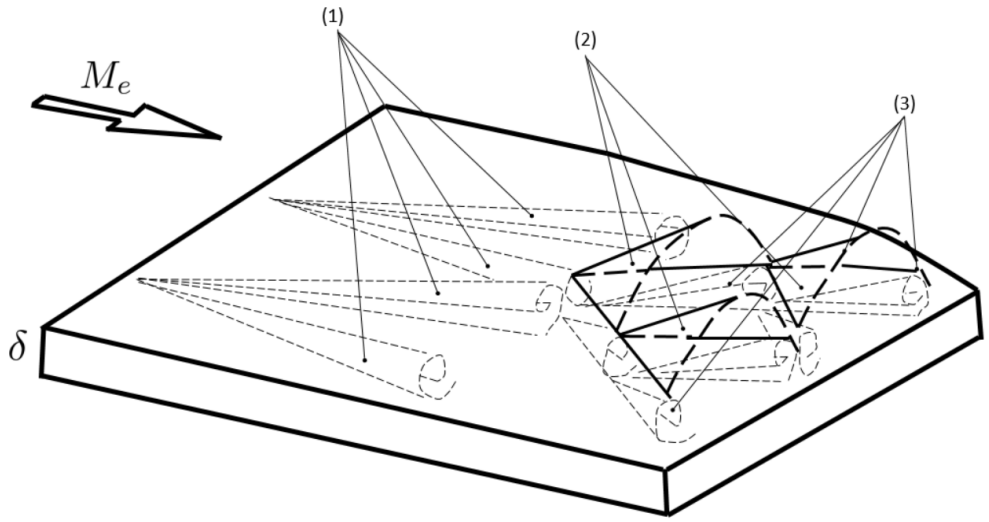

Figure 2.7: Sketch of flow model of cross-hatching. (1) Vortices alone edges of ablation wedges, (2) conical shock waves caused by growth of vortices, (3) Vortices along edges of cross-hatching. [16]

2.5 Surface Deformation Mechanism

Probstein and Gold proposed a surface deformation mechanism. They believed crosshatching is the result of differential deformation due to relaxation and creep and does not require an ablative material [17][32]. They proposed that the patterns formed result

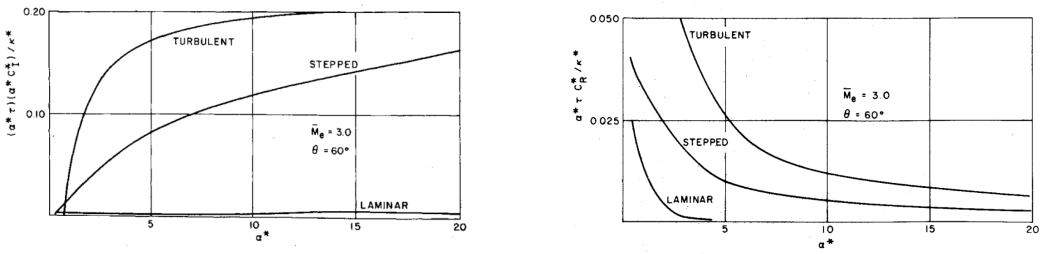

(a) Amplification Rate (b) Disturbance wave speed

Figure 2.8: Example result of Probstein and Gold Stability Analysis for different boundary-layer types [17]

from an interaction between the shear stress fluctuations in a turbulent boundary layer at the wall and a viscous deformable body. Through stability calculations, they show the effects on the surface pattern characteristics of different boundary layer profiles. They consider the Maxwell deformable-surface models and show the amplification rate as a function of wave-number for laminar and turbulent boundary layers. The stability analysis showed that the turbulent profiles result in a stronger disturbance wave speed and amplification rate[17].

To test the surface-deformation postulate, Stock and Ginoux tested two 13^0 half-angle wax cones in a Mach 5.3 wind tunnel[33]. The cones were of different initial ablation material temperatures (290K and 332K), where the highest temperature was near the liquefaction temperature. Stock and Ginoux's experiments showed larger patterns for the wax model at the higher temperature. There is a slight variation in the boundary-layer properties at the test temperature range, material density, specific heat, and thermal conductivity. However, the viscosity and shear modulus for wax show considerable variation in this temperature range, indicating the viscosity is an essential parameter in the formation of crosshatching. Probstein and Gold's also tested the deformation theory by Nachtsheim[18]. The model tested was a 40^0 half-angle Teflon (FEP) cone shown in Figure 2.9. The test conditions selected by Nachtsheim were such that the model did not ablate. The post and pre-weights of the module indicated no mass loss and yet still had visible crosshatching patterns and therefore supports the hypothesis by Probstein and Gold that crosshatching can occur in the absence of ablation.

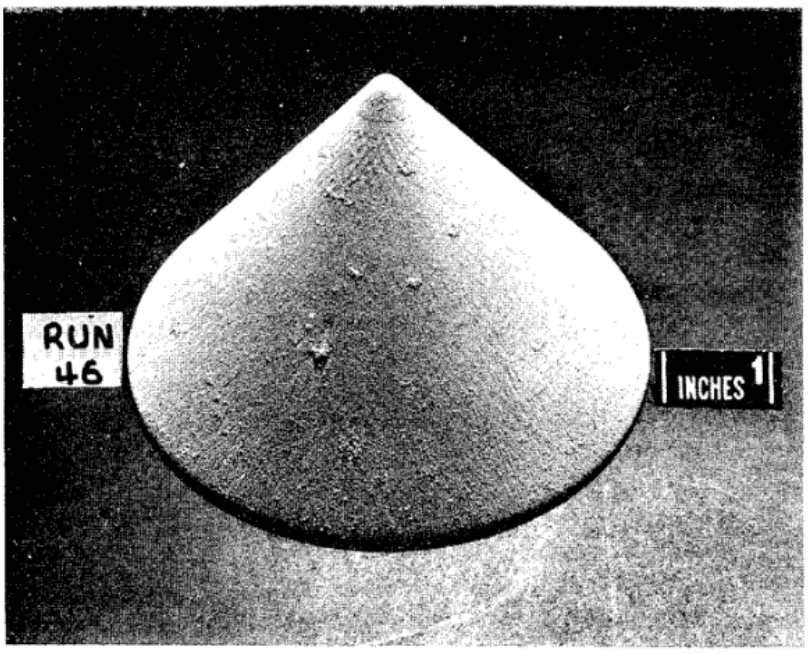

Figure 2.9: Crosshatching on 40^0 Teflon (FEP) cone tested at NASA Ames [18]

2.6 Summary and Discussion

The postulated mechanisms presented here include vortex initiation, groove marching process, vortex turbulent wedge interaction, surface deformation instabilities, and liquid layers instabilities. All mechanisms have viable evidence of crosshatching initiation but fall short to explain the mechanism fully. The initiation of pattern development due to streamwise vortices was deemed invalid by Stock and Ginoux. Stock and Ginoux placed a single row of three-dimensional roughness elements of varying height diameters and spacing to introduce vortices of different intensities. They observed that patterns were essentially unchanged and only had a local effect. Laganelli and Zempel also investigated the groove marching mechanism. Similar to Stock and Ginoux, they placed roughness elements on a model, except they placed multiple rows and columns trying to mimic the propagation of Mach cones. They also observed that only a local effect similar to Stock and Ginoux and did not affect the overall pattern development. The liquid layer instability is too specific. Not all the materials that exhibited the crosshatching pattern liquefy under the conditions tested in the literature. The experiments conducted by

Langanelli to understand if crosshatching is due to a surface deformation instability and not ablation had a bead of Teflon around the edges of the base after the test indicating an ablation process occurred. The verdict is still out of whether or not differential surface deformation in the absence of material ablation or surface melt is a viable mechanism and open for discussion. The progression of pattern development shown in Qun's experiments is interesting. Qun noted the presence of pits before the formation of turbulent wedges and then crosshatching. The pits could be an apex of Mach cones that eventually interact with streamwise vortices, similar to the postulate by Tobak, and the patterns would then form from the Mach cone and streamwise vortex interaction.

Chapter 3

Governing Equations

3.1 Introduction

The simulations performed for this work uses a low-temperature ablation material, camphor. A low-temperature material is ideal for wind tunnel tests where long run times are required to study ablation. As the solid camphor heats up, it undergoes a phase change from solid to gas. The sublimation process injects mass into the flow, and the flowfield now has multiple species of camphor gas and air. Although there is no flowfield chemistry because the camphor gas and air molecules are not reacting, the two species flow changes the mixture thermodynamics and transport properties to be different from a perfect gas mixture when only considering a single gas. This chapter presents the governing equations that account for mass transport and diffusion of the multiple species gas relevant to this work.

3.2 Flowfield Conservation Equations

The Navier-Stokes equations are a set of partial differential equations that describe the motion of viscous fluids. They consist of the conservation of mass, momentum, and energy equations. Consider a multi-species laminar flow and a fluid flow with a mixture of ns species; there are ns mass conservation of equations of the form

$$\frac{\partial \rho_s}{\partial t} + \frac{\partial}{\partial x_j}(\rho_s u_j) + \frac{\partial}{\partial x_j}(\rho_s v_{sj}) = w_s, \tag{3.1}$$

where ρ_s is the density and v_{sj} is the diffusion velocity of each species, and for this work, the chemical source term w_s due reactions is zero. The method to evaluate the diffusion velocity for a binary system will be discussed in section 3.4. The total momentum equations for gas mixture take the form

$$\frac{\partial}{\partial t}(\rho u_i) + \frac{\partial}{\partial x_j}(\rho u_i u_j + p\delta_{ij}) + \frac{\partial}{\partial x_j}(\tau_{ij}) = 0, \tag{3.2}$$

The stress tensor τ_{ij} is derived assuming a Newtonian fluid and given by Equation 3.3 where μ is the kinematic viscosity of the mixture calculated using Wilke's mixing rule [34].

$$\tau_{ij} = -\mu\left(\frac{\partial u_i}{\partial x_j} + \frac{\partial u_j}{\partial x_i}\right) + \frac{2}{3}\mu\frac{\partial u_k}{\partial x_k}\delta_{ij}, \tag{3.3}$$

The final equation, the total energy equation, is given by Equation 3.4 where h_s is the species enthalpy per unit volume, and q_j is the heat conduction term given by Fourier's Law.

$$\frac{\partial E}{\partial t} + \frac{\partial}{\partial x_j}\left((E+p)u_j\right) + \frac{\partial}{\partial x_j}q_j + \frac{\partial}{\partial x_j}\tau_{ij}u_i + \sum_{s=1}^{ns}\frac{\partial}{\partial x_j}(h_s v_{sj}) = 0. \tag{3.4}$$

3.3 Equations of State

The total energy of gas per unit volume is defined by Equation 3.5 where c_{vs} is the translational-rotational specific heat and h_s^o is the heat of formation species s.

$$E = \sum_{s=1}^{ns}\rho_s c_{vs}T + \frac{1}{2}\rho(u_i u_i) + \sum_{s=1}^{ns}\rho_s h_s^o \tag{3.5}$$

The equation of state that defines the thermodynamic static pressure is related to the temperature and partial pressures of each species using Dalton's Law.

$$p = \sum_{s=1}^{ns}\frac{\rho_s RT}{M_s} \tag{3.6}$$

3.4 Species Mass Transport Model

The diffusion velocities, $v_{s,j}$, used in the species mass conservation Equation 3.1 and conversation of energy Equation 3.4 are calculated using a mass transport model. For this work multiple species, camphor and air, are considered and for a binary mixture Fick's law of diffusion in terms of mass fraction gradient is defined by

$$J_i = -\rho \mathcal{D}_{ij} \nabla c_i \tag{3.7}$$

where $\mathcal{D}_{ij}$ is the diffusion coefficient between the species and c_i is mass fraction of species i [35, 36]. The diffusion coefficient is obtained by curve fits and available for camphor and air in Appendix C. Fick's Law in terms of mole fraction gradient by,

$$J_i = -\rho \frac{M_i}{M} \frac{M_j}{M} \mathcal{D}_{ij} \nabla x_i \tag{3.8}$$

where M_i is the molecular weight of species i and M is the average molecular weight of the mixture defined by

$$M = \sum_i \chi_i M_i \tag{3.9}$$

For a system containing two species camphor and air the mole fraction gradient ∇x_i can then be simplified according to Bird [35].

$$\nabla x_i = \frac{\dfrac{1}{M_i M_j} \nabla c_i}{\left(\dfrac{c_i}{M_i} + \dfrac{c_j}{M_j} \right)^2} \tag{3.10}$$

3.5 Transport Properties

The total mixture viscosity coefficient, μ, is calculated by finding the viscosity for each species in the gas mixture and then applying a mixing rule. For air, the viscosity coefficient is determined by using the curve fits obtained by Blottner et al. [37].

$$\mu_{air} = 0.1 \exp[(A_{air} + B_{air}) \ln T + C_{air}]. \tag{3.11}$$

where A_{air}, B_{air}, and C_{air} are species dependent curve fit coefficients. The viscosity of the camphor gas species is provided by Yaw's Handbook curve fits listed in Appendix C [38]. The total viscosity of the camphor vapor-air gas mixture is calculated using Wilke's semi-empirical mixing rule derived from kinetic theory [34].

$$\mu = \sum_{s=1}^{ns} \frac{X_s \mu_s}{\phi_s} \tag{3.12}$$

where X_s and ϕ_s are defined by Equation 3.13 and 3.14 and r is air when evaluating ϕ_s for camphor and r is air when evaluating ϕ_s for air.

$$X_s = \frac{C_s M}{M_s} \tag{3.13}$$

$$\phi_s = \sum_{s=1}^{ns} X_r \left[1 + \sqrt{\frac{\mu_s}{\mu_r}} \left(\frac{M_r}{M_s} \right)^{1/4} \right]^2 \left[\sqrt{8 \left(1 + \frac{M_s}{M_r} \right)} \right]^{-1} \tag{3.14}$$

$$M = \left(\sum_{s=1}^{ns} \frac{C_s}{M_s} \right)^{-1} \tag{3.15}$$

Fourier's Law defines the flux vector given by Equation 3.16 and the total thermal conductivity, k, is obtained similar to the total viscosity by Wilke's semi-empirical assumption. The thermal conductivity for air is related to the viscosity by a constant Prandtl number, and a curve fit is used for the camphor gas and provided in Appendix C.

$$q_j = -k \frac{\partial T}{\partial x_j} \tag{3.16}$$

$$\kappa = \sum_{s=1}^{ns} \frac{X_s \kappa_s}{\phi_s} \tag{3.17}$$

Chapter 4

Numerical Methods

4.1 Spatial Discretization

The finite volume formulation evaluates the Navier-Stokes equations in the form of algebraic equations. The equations are solved on a domain made of control volumes generated from computational meshes. For each mesh face, a flux is evaluated for mass, momentum, and energy. The fluxes entering a control volume balances the fluxes leaving the control volume, making this method conservative. The conservation equations for each cell of many faces can be written in the partially discrete form given by Equation 4.1.

$$\frac{\partial \bar{U}}{\partial t} = -\frac{1}{V} \sum_{f} \left(\vec{F} \cdot \hat{n} \right) S \tag{4.1}$$

The numerical methods used to solve the Navier-Stokes equations are presented in the following sections. Here and further, the subscripts 1 and 2 refer to air and the camphor vapor, respectively. The flux at each face is divided into its inviscid and viscous portions. Each component is then treated differently numerically due to the nature of the equations. The subscripts I and V indicate inviscid and viscous fluxes, respectively.

The flux vector in Cartesian components is given by

$$\vec{F} = F\hat{i} + G\hat{j} + H\hat{k} \tag{4.2}$$

and the components for the inviscid and viscous flux are given in Equation 4.3- 4.4.

$$F_I = \begin{bmatrix} \rho u_1 \\ \rho u_2 \\ \rho uu + p \\ \rho uv \\ \rho uw \\ (E+p)u \end{bmatrix}, G_I = \begin{bmatrix} \rho v_1 \\ \rho v_2 \\ \rho uv \\ \rho vv + p \\ \rho vw \\ (E+p)v \end{bmatrix}, H_I = \begin{bmatrix} \rho w_1 \\ \rho w_2 \\ \rho uw \\ \rho vw \\ \rho ww + p \\ (E+p)w \end{bmatrix}. \tag{4.3}$$

$$F_V = \begin{bmatrix} \rho \mathcal{D} \frac{\partial c_1}{\partial x} \\ \rho \mathcal{D} \frac{\partial c_2}{\partial x} \\ \tau_{xx} \\ \tau_{xy} \\ \tau_{xz} \\ q_x + \tau_{xx}u + \tau_{xy}v + \tau_{xz}w + \rho \sum_{ns} h_s \mathcal{D} \frac{\partial c_s}{\partial x} \end{bmatrix},$$

$$G_V = \begin{bmatrix} \rho \mathcal{D} \frac{\partial c_1}{\partial y} \\ \rho \mathcal{D} \frac{\partial c_2}{\partial y} \\ \tau_{xy} \\ \tau_{yy} \\ \tau_{yz} \\ q_y + \tau_{xy}u + \tau_{yy}v + \tau_{yz}w + \rho \sum_{ns} h_s \mathcal{D} \frac{\partial c_s}{\partial y} \end{bmatrix},$$

$$H_V = \begin{bmatrix} \rho \mathcal{D} \frac{\partial c_1}{\partial z} \\ \rho \mathcal{D} \frac{\partial c_2}{\partial z} \\ \tau_{xz} \\ \tau_{yz} \\ \tau_{zz} \\ q_z + \tau_{xz}u + \tau_{yz}v + \tau_{zz}w + \rho \sum_{ns} h_s \mathcal{D} \frac{\partial c_s}{\partial z} \end{bmatrix}. \tag{4.4}$$

4.1.1 Evaluation of Inviscid Fluxes

The inviscid fluxes are hyperbolic, which means fluid properties propagate along with the characteristics lines. A method to solve the hyperbolic portion of the governing

equations is the use of up-winding numerical methods. The discretization of the equations is performed according to the direction of propagation. For this work, the Steger and Warming formulation is used, which is one of the first characteristic-based flux schemes to ensure stability [39].

Steger-Warming Formulation

Steger and Warming scheme leverage the property that the inviscid fluxes are homogeneous in the vector of conserved variables U, and this property forms the basis for flux vector splitting numerical scheme. The homogeneity of $\vec{F}$ allows the flux vector to be linearized and written as the product of the Jacobian matrix A and the vector of conserved variables U.

$$\vec{F} = \frac{\partial \vec{F}}{\partial U} U = AU \tag{4.5}$$

The Steger-Warming formulation splits the fluxes according to the signs of the eigenvalues of the Jacobians[40]. The eigenvalue decomposition of A is required but is difficult to compute in this form. A transformation of the conservative Jacobians into the non-conservative form simplifies the calculation and the non-conservative variables are given by

$$V = (\rho_1, \rho_2, u, v, w, p)^{'} \tag{4.6}$$

The Jacobian matrix A can be written in terms of transformation matrices between the conserved and primitive variables where $\frac{\partial U}{\partial V}$ and $\frac{\partial V}{\partial U}$ and are denoted by S^{-1} and S.

$$A = \frac{\partial F}{\partial U} = \frac{\partial U}{\partial V}\frac{\partial V}{\partial U}\frac{\partial F}{\partial V}\frac{\partial V}{\partial U} = S^{-1}\frac{\partial V}{\partial U}\frac{\partial F}{\partial V}S \tag{4.7}$$

The matrix $\frac{\partial V}{\partial U}\frac{\partial F}{\partial V}$ is now easier to diagonalize than the original matrix A and composed of the eigenvalues Λ and the eigenvectors R^{-1} and R.

$$\frac{\partial F}{\partial U} = \frac{\partial U}{\partial V}R^{-1}\Lambda R\frac{\partial V}{\partial U} = S^{-1}R^{-1}\Lambda RS \tag{4.8}$$

After the transformation is applied, the inviscid flux can now be split into positive and negative parts.

$$F = F_+ + F_- \tag{4.9}$$

$$F_+ = S^{-1}R^{-1}\Lambda_+ RSU = A_+ U \tag{4.10}$$

$$F_- = S^{-1}R^{-1}\Lambda_- RSU = A_- U \tag{4.11}$$

where $\Lambda_\pm$ are the diagonal matrices of positive and negative eigenvalues. The positive and negative eigenvalues are given by

$$\Lambda_+ = \frac{1}{2}(u^{'} + |u^{'}|),\ \Lambda_+ = \frac{1}{2}(u^{'} \pm a + |u^{'} \pm a|) \tag{4.12}$$

$$\Lambda_- = \frac{1}{2}(u^{'} - |u^{'}|),\ \ \Lambda_- = \frac{1}{2}(u^{'} \pm a - |u^{'} \pm a|) \tag{4.13}$$

A modification to the scheme is made by averaging the values of the cells at the flux face allowing the scheme to have less dissipation [41]. This modification has less dissipation but now has problems when the eigenvalues are close to zero near the sonic line or stagnation points. A correction with a fraction of the speed of sound is added to the eigenvalues to avoid numerical issues.

Higher-order upwind schemes are another method to resolve features in the flow otherwise smeared out by numerical dissipation. These methods require a larger stencil and are subject to nonphysical oscillations near shocks or large gradients. A flux limiter can be used to avoid numerical oscillations, add dissipation in the vicinity of shock waves, and reverts to first-order numerics.

Shock Capturing Methods

Shock-capturing methods are another method to reduce dissipation in the solution. This scheme selectively adds numerical dissipation in regions of shocks or large gradients. The flux splitting method discussed in section 4.1.1 can be split into symmetric and dissipative components, which allows the fluxes to be treated differently depending on the flow characteristics.

$$F = F_{symm} + \alpha_{diss} F_{diss} \tag{4.14}$$

The first term on the right-hand side is the symmetric part of the modified Steger–Warming flux, and the second term is the non-dissipative part. The non-dissipative part is replaced with the kinetic energy consistent (KEC) flux developed by Subbareddy and Candler, which uses a gradient reconstruction to produce a sixth-order accurate flux[42]. The α_{diss} term is the numerical switch that allows the scheme to add in dissipative when necessary. Numerical switches take many forms and are selected based on the computational problem. The present work uses the Larsson switch, defined by Equation 4.15 where ω_i is the vorticity, c is the speed of sound, and h the cell size[43].

$$\alpha_{diss} = \begin{bmatrix} 0, \theta_L \leq 1 \\ 1, \theta_L > 1 \end{bmatrix} \tag{4.15}$$

$$\theta_L = \frac{-(\nabla \cdot u_i)}{max\left(1.5\sqrt{\omega_i \omega_i}, 0.05\left(\frac{c}{h}\right)\right)} \tag{4.16}$$

4.1.2 Evaluation of Viscous Fluxes

The viscous fluxes are elliptical and depend on spatial derivatives to calculate the shear-stress, heat flux, and species diffusion terms. Their evaluation requires an approximation of gradients at each control volume. One method is the weighted least square gradient reconstruction. This method solves for the values of the gradients by solving a minimization problem. The weighted least square reconstruction method and the interpolation method required to solve for the gradients at cell faces are described in greater detail by Drayna [44].

4.2 Time Integration

The temporal derivative in the Navier-Stokes equations needs to be solved to advance the solution in time. There are two methods to solve the time integration: explicit and implicit. The explicit method has a time step limitation, and the implicit method overcomes the explicit time integration limitations by taking more significant time steps suitable for solving steady-state problems marching in time while maintaining stability.

There are many implicit methods discussed in detail by Nompelis [45, 46]. The data-parallel line relaxation method, developed by Wright, is common method used to speed up convergence and the implicit method of choice for this work [47].

For the implicit method, the solution at any point depends on the solution of all other points at the future time level n+1. This coupling creates an extensive linear algebraic equations system; however, considering the nature of flowfield allows for the large set of algebraic equations to be solved efficiently.

4.2.1 Implicit Evaluation of Inviscid Fluxes

The implicit formulation of the inviscid method requires the linearization of the inviscid fluxes.

$$F_{i,j}^{n+1} = F_{i,j}^{n} + \frac{\partial F}{\partial U}^{n}_{i,j} (U_{i,j}^{n+1} - U_{i,j}^{n}) + \mathcal{O}(\Delta t^2) \tag{4.17}$$

$$F_{i,j}^{n+1} \simeq F_{i,j}^{n} + A_{i,j}^{n} \delta U_{i,j}^{n} \tag{4.18}$$

where $A_{i,j}$ is the inviscid full Jacobian and $\delta U_{i,j}$ is the difference of the conserved variables at time level n and $n+1$. The fully implicit formulation takes the form:

$$\delta U_{i,j} = -\frac{\Delta t}{V_{i,j}} \sum_{faces} F^{n+1} S \tag{4.19}$$

Like the Steger-Warming formulation, the Jacobians are split into positive and negative components instead of the full Jacobian. Substituting the linearized fluxes, we obtain an expression that is only a function of data at the current time level, n.

$$\delta U_{i,j}^{n} + \frac{\Delta t}{V_{i,j}} \sum_{faces} A^{n} S \delta U_{f}^{n} = -\frac{\Delta t}{V} \sum_{faces} F^{n} S \tag{4.20}$$

In matrix form, the solution to these systems of equations becomes a large block pentadiagonal linear algebraic problem. An approach to solve this matrix is to consider the physics of the flow to simplify the matrix inversion. When building a computational mesh, the lines are aligned with the flow direction and boundary layer growth. An accurate solution in the boundary layer direction is required, while a less coupled

approach is allowed for the flow direction. The matrix is rearranged to form a less coupled approach in the flow direction. This approach requires an iterative scheme to solve for $\delta U_{i,j}$ at each next time level $n+1$.The Gauss-Seidel line-relaxation inversion and iteration method are used because it converges well for strictly diagonally dominated matrices. The matrix solves now consists of an inversion is now simplified to a block tri-diagonal inversion with alternating sweeps in the backward and forward flow or i directions. For the first sweep, $\delta U_{i,j}^{(0)}$ is set to zero, and for steady-state simulations, only a few backward and forwards sweeps are required to reach convergence. The block diagonal implicit matrix is given by

$$\begin{bmatrix} & & & & & & & & & \\ \ddots & & \ddots & \ddots & \ddots & & \ddots & & & \\ & \hat{E}_{i,j} & & \hat{C}_{i,j} & \hat{A}_{i,j} & \hat{B}_{i,j} & & \hat{D}_{i,j} & & \\ & & \ddots & & \ddots & \ddots & \ddots & & \ddots & \\ & & & & & & & & & \end{bmatrix} \begin{bmatrix} \delta U_{1,1} \\ \vdots \\ \delta U_{i,j} \\ \vdots \\ \delta U_{Ni,Nj} \end{bmatrix}^n = \begin{bmatrix} \Delta U_{1,1} \\ \vdots \\ \Delta U_{i,j} \\ \vdots \\ \Delta U_{Ni,Nj} \end{bmatrix}^n \tag{4.21}$$

and the inviscid Jacobians for the implicit formation are defined by

$$\hat{A}_{i,j} = I + \frac{\Delta t}{V_{i,j}}(A'_{+,i,j}S_{i+1/2,j} + A'_{+,i,j}S_{i,j+1/2} - A'_{-,i,j}S_{i-1/2,j} - A'_{-,i,j}S_{i,j-1/2}) \tag{4.22}$$

$$\hat{B}_{i,j} = \frac{\Delta t}{V_{i,j}}(A'_{-,i,j+1}S_{i,j+1/2}) \tag{4.23}$$

$$\hat{C}_{i,j} = \frac{\Delta t}{V_{i,j}}(A'_{+,i,j-1}S_{i,j-1/2}) \tag{4.24}$$

$$\hat{D}_{i,j} = \frac{\Delta t}{V_{i,j}}(A'_{-,i+1,j}S_{i+1/2,j}) \tag{4.25}$$

$$\hat{E}_{i,j} = \frac{\Delta t}{V_{i,j}}(A'_{+,i-1,j}S_{i+1/2,j}) \tag{4.26}$$

4.2.2 Implicit Evaluation of Viscous Fluxes

The viscous formation for the implicit solve utilizes the thin-layer assumption, which implies the gradients in the normal direction are much larger than the gradients in the

flow direction. A grid constructed with the grid lines properly aligned with strong gradients such as shocks and boundary layers, the η direction is along the strong gradients, and ξ is parallel to the flow. The viscous flux is approximated using only the gradients normal to the wall which dominate.

$$G_v \simeq M_\eta \frac{\partial V}{\partial \eta} \tag{4.27}$$

That matrix M_η is a function of transport and grid properties, and V is a vector of the primitive variables density, velocity, and temperature. The primitive vector is converted to the conserved variables by defining the Jacobian matrix $N = \frac{\partial V}{\partial U}$. The viscous flux in the body-normal direction is now approximated by

$$G_v \simeq M_\eta \frac{\partial NU}{\partial \eta} \tag{4.28}$$

The viscous flux approximation is now linearized in time and simplified to assume that non-derivative terms are locally constant.

$$\begin{aligned} G_v^{n+1} &\simeq G_v^n + \delta G_v^n && (4.29)\\ &\simeq G_v^n + \delta \left(M_\eta N \frac{\partial U^n}{\partial \eta} \right) && (4.30)\\ &\simeq G_v^n + M_\eta N \frac{\partial \delta U^n}{\partial \eta} && (4.31) \end{aligned}$$

The block tri-diagonal matrix for the implicit formation now includes the viscous terms.

$$\begin{aligned} \hat{A}_{i,j} = I + \frac{\Delta t}{V_{i,j}} (& A'_{+,i,j} S_{i+1/2,j} + A'_{+,i,j} S_{i,j+1/2} - A'_{-,i,j} S_{i-1/2,j} - A'_{-,i,j} S_{i,j-1/2} \\ & - M_{\eta i,j+1/2} N_{i,j+1/2} S_{i,j+1/2} - M_{\eta i,j-1/2} N_{i,j-1/2} S_{i,j-1/2})^n \end{aligned} \tag{4.32}$$

$$\hat{B}_{i,j} = + \frac{\Delta t}{V_{i,j}} (A'_{-,i,j+1} S_{i,j+1/2} + M_{\eta i,j+1/2} N_{i,j+1/2} S_{i,j+1/2})^n \tag{4.33}$$

$$\hat{C}_{i,j} = - \frac{\Delta t}{V_{i,j}} (A'_{+,i,j-1} S_{i,j-1/2} + M_{\eta i,j-1/2} N_{i,j-1/2} S_{i,j-1/2})^n \tag{4.34}$$

4.3 Ablation Boundary Condition

An ablation boundary condition is implemented into an unstructured finite volume Naiver-Stokes Solver US3D which allows simulation of the shape change and the correct wall temperature [48]. The ablation material of choice is camphor which undergoes sublimation at low temperatures. A boundary condition is used to couple the camphor solid and the surrounding flow field, and is this coupling is performed through a surface mass balance and a surface energy balance equations. The boundary condition is then validated using experimental results and discussed in the next chapter.

A novel feature of US3D is performing dynamic grid motion simulations while maintaining grid quality, even after significant levels of grid deformation. The complete mathematical details of the approach are provided by Gidzak[49]. Conceptually, the grid is constrained to follow rigid-body motion near moving solid surfaces to preserve the near-wall grid spacing. In non-near-wall regions, the grid deforms through a combination of rigid-body translation, rigid-body rotation, and compression. The grid deformation is enforced at grid nodes, not element centroids, which is crucial for maintaining grid quality and preventing high-frequency instabilities in the grid[50].

4.4 Mass Balance

The surface mass-energy balance for a sublimation material is shown in Figure 4.1. Due to the conservation of total mass and mass of each species, the mass flux of k species leaving the volume by blowing balances the mass flux entering the infinitesimal control volume by diffusion or due to surface reactions. The surface mass balance in Figure 4.1 can be written in Equation 4.35 where k is the value of two for air and camphor.

$$\underbrace{\rho D_k \frac{\partial \gamma_k}{\partial \eta}\Big|_w}_{\text{Diffusion}} + \underbrace{\dot{\omega}_k}_{\text{Sublimation rate}} = \underbrace{(\rho v)_w c_k}_{\text{Blowing}} \tag{4.35}$$

The sublimation rate for camphor is modeled by with the Knudsen-Langmuir Equation 4.36 where α is a constant vaporization coefficient (taken as $\alpha = 0.18$)[51], the subscript c indicates camphor quantities, and p_{vc} is the vapor pressure of camphor. The

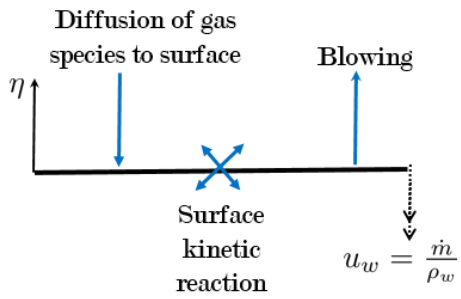

Figure 4.1: Surface mass balance

vapor pressure for camphor is defined as the pressure exerted by a vapor in thermodynamic equilibrium with its solid phase at a given temperature in a closed system.

$$\dot{\omega}_2 = \alpha \sqrt{\frac{M_c}{2\pi R T_w}} (p_{vc} - p_2) \tag{4.36}$$

A model for camphor vapor pressure was obtained from reference [52] and the following expression was used:

$$p_{vc} = \exp\left(13.630 - \left(\frac{6441.5}{T_w}\right)\right) \text{atm.} \tag{4.37}$$

4.5 Energy Balance

The surface balances are derived through the assumption of conservation of total energy, and the surface balance for a sublimation material is shown in Figure 4.2. The energy flux of k species entering the volume by convection, solid enthalpy, diffusion is balanced by the energy flux leaving the wall by surface radiation, conduction in the solid, and carried away by the sublimation gas leaving the surface.

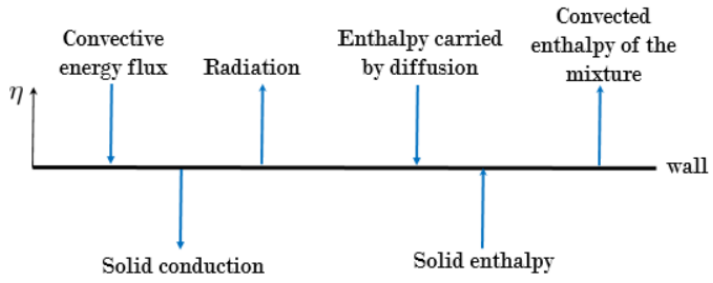

Figure 4.2: Surface energy mass balance

The surface energy balance shown in Figure 4.2 can be written as

$$\underbrace{\kappa \frac{\partial T}{\partial \eta}\Big|_w}_{\text{Convection}} + \underbrace{\sum_k \rho D_k h_k \frac{\partial \gamma_k}{\partial \eta}\Big|_w}_{\text{Diffusion}} + \underbrace{\dot{m}_w h_{s,w}}_{\text{Solid enthalpy}} = \underbrace{q_{c_w}}_{\text{Conduction}} + \underbrace{q_{rad_{out}}}_{\text{Radiation}} + \underbrace{(\rho v)_w h_w}_{\text{Blowing}} \tag{4.38}$$

where $h_{s,w}$ is the enthalpy of the solid camphor at the surface temperature, and h_w is the enthalpy of the air and camphor gases.

The camphor mass balance and energy balance equations are solved in a coupled fashion using a Newton iteration on the wall temperature, T_w. During this solution, the thermos-chemical state of the gas in the element closest to the wall and the temperature in the solid are held fixed. The wall pressure is assumed to be equal to that of the gas in the nearest element.

Chapter 5

Baker Validation Study

The Baker experiments studied camphor models in a laminar and turbulent environment at the Naval Ordnance Laboratory (NOL) [19]. The model is a 2.5 in nose radius, 8^o half-angle cone, 9.4 inches in length, and the tunnel freestream conditions are provided in Table B.1.

Mach	To	Po	AoA
–	[K]	[MPa]	[deg]
5.00	797	0.8	0

Table 5.1: Baker Laminar Tunnel Conditions for Validating US3D

At these conditions, the flow is fully laminar and was used to validate the camphor boundary condition in US3D. The pre-test and post-test photographs are shown in Figure 5.1. The experimental body shape was measured at different time intervals and compared to theoretical predictions based on analysis by Welsh [53].

The workflow to run a coupled steady-state ablation calculation is provided in Figure 5.2. The process begins with generating fluid and solid mesh that is point-matched. The fluid solution is converged to an initial condition with a cold or an adiabatic wall. Once the fluid is fully converged, the ablation boundary condition is applied, and a new wall temperature and species concentrations are calculated. The solid solver then solves for the conduction through the wall with a new prescribed surface temperature then the solid and fluid mesh is moved to account for camphor sublimating.

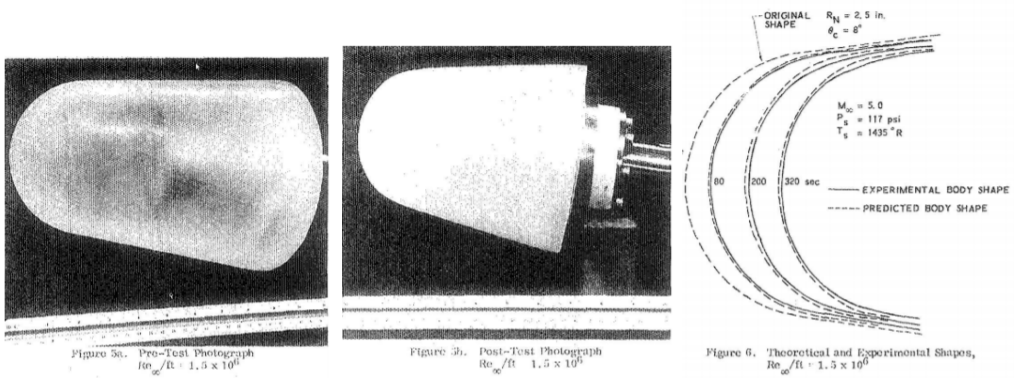

Figure 5.1: Test Photographs and Experimental Shapes

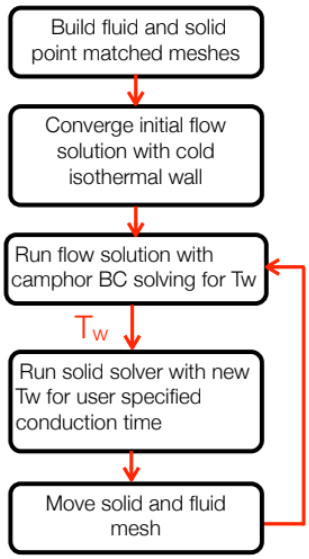

Figure 5.2: Coupled Fluid-Solid Simulation Process

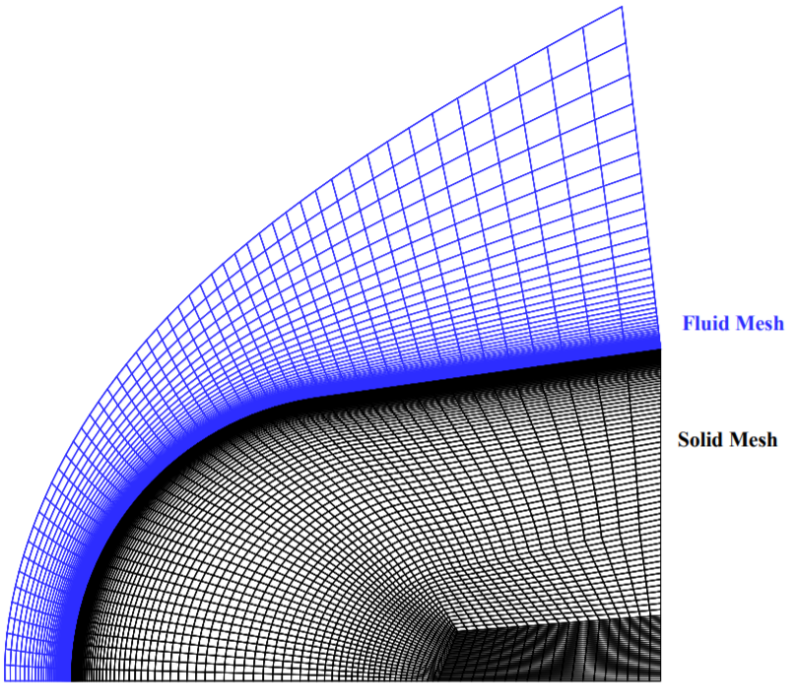

Figure 5.3: Original Fluid Solid Mesh

The original computational grid for both the fluid and solid is shown in Figure 5.3. Note that the two meshes are point matched at the fluid-solid interface. After 260 seconds, the solid recessed a considerable amount; Figure 5.4 is a plot of the surface mesh and temperature compared to the original shape of the solid. The computed temperature distribution in the fluid and on the surface at the final run time of 320 seconds and the density of camphor is shown in Figure 5.5. Notice there is a thin region above the surface where the camphor density is high. The molecular weight of camphor gas is very large, which causes the molecules to have low mass diffusivity, and as a result, they stay close to the surface.

Comparisons between the shape change of the ablation boundary condition and the experiments are also shown in Figure 5.6 at 80 seconds (blue), 200 seconds (green), and 320 (orange) seconds. The stagnation point and side wall recession are in very good agreement with the experimental data.

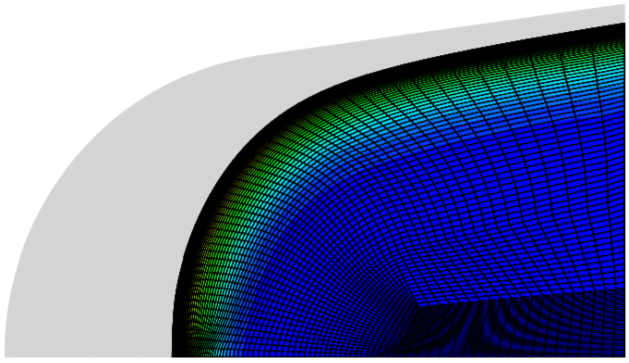

Figure 5.4: Plot of surface mesh and temperature after 260 seconds of ablation compared to original shape of the solid

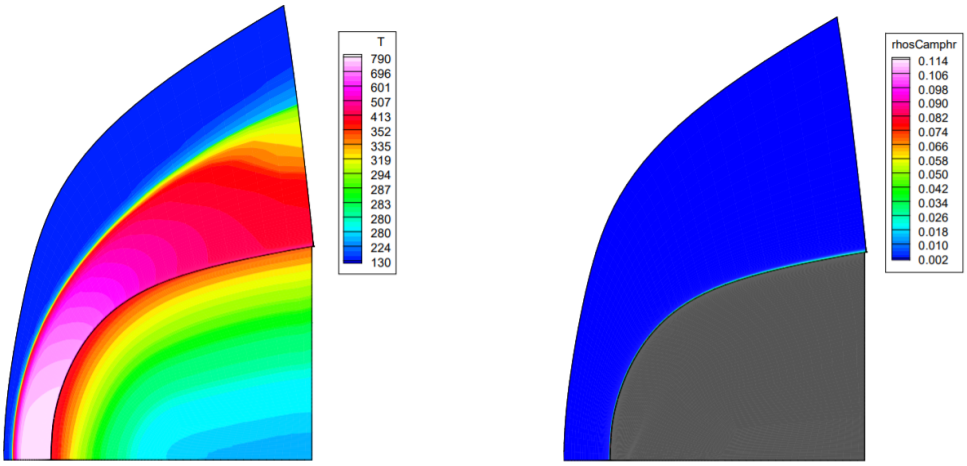

(a) Temperature

(b) Camphor Density

Figure 5.5: Computed temperature in fluid and surface and computer camphor density in the fluid

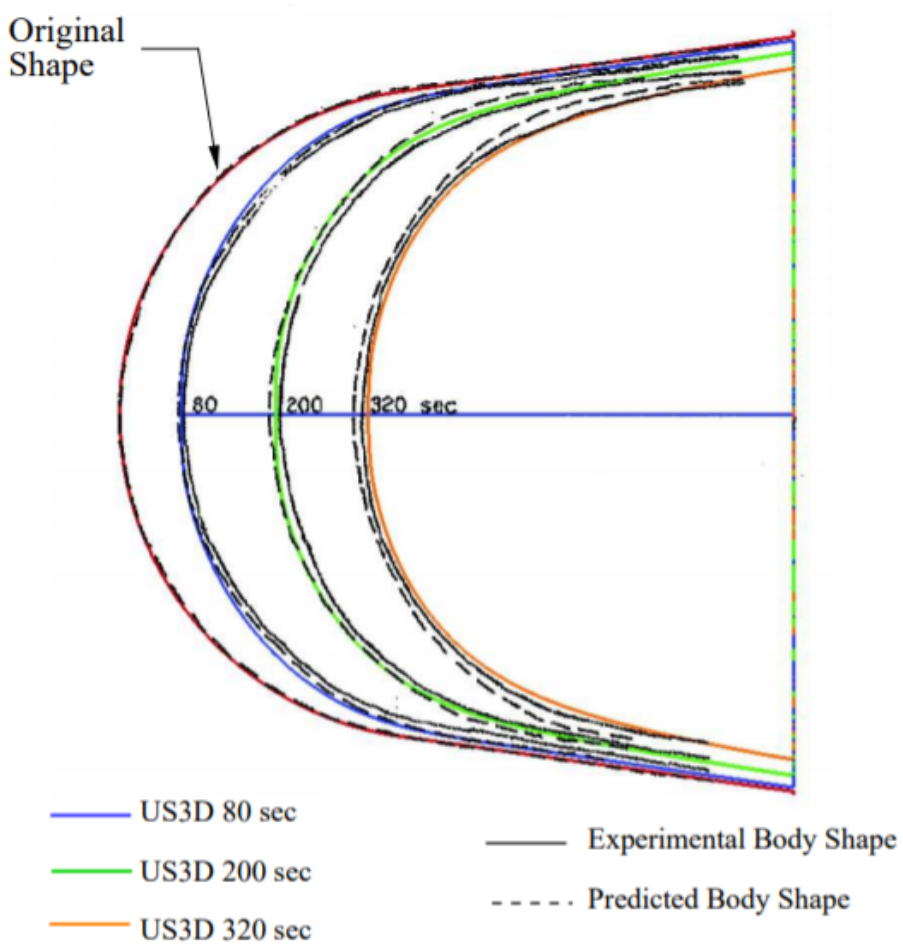

Figure 5.6: Comparison of US3D Results and NOL Shape Data from Baker [19]

Chapter 6

Numerical Approach

6.1 Stock Geometry and Flow Conditions

Stock and Ginoux performed an extensive experimental study at the VKI H-1 facility to understand the possible mechanisms to initiate crosshatching. Two of the Stock geometry configurations, a cone, and a flat plate, are analyzed using the ablation boundary condition and moving mesh capability in US3D. The freestream conditions chosen for both models are tabulated in Table 6.1. The test articles contain a steel tip to prevent recession and wax as the ablative material. The cone is a 13^0 half-angle cone, with a 6cm steel tip and 30cm long at the angle of attack, and the flat plate was a much smaller model with a 1cm steel leading edge and 14cm long. For this work, a camphor model was implemented and validated with US3D; therefore, the low-temperature ablator is camphor for these simulations. There is minimal data and images of camphor models, and since the patterns were observed for all types of materials at similar conditions replacing wax with camphor was justified. The computational objective of both simulations is discussed further.

Geometry	Mach	To[K]	Po[MPa]	AoA [deg]
Flat Plate	5.3	399	3.0	10
13^0 Cone	5.3	399	3.0	0

Table 6.1: Tunnel Conditions

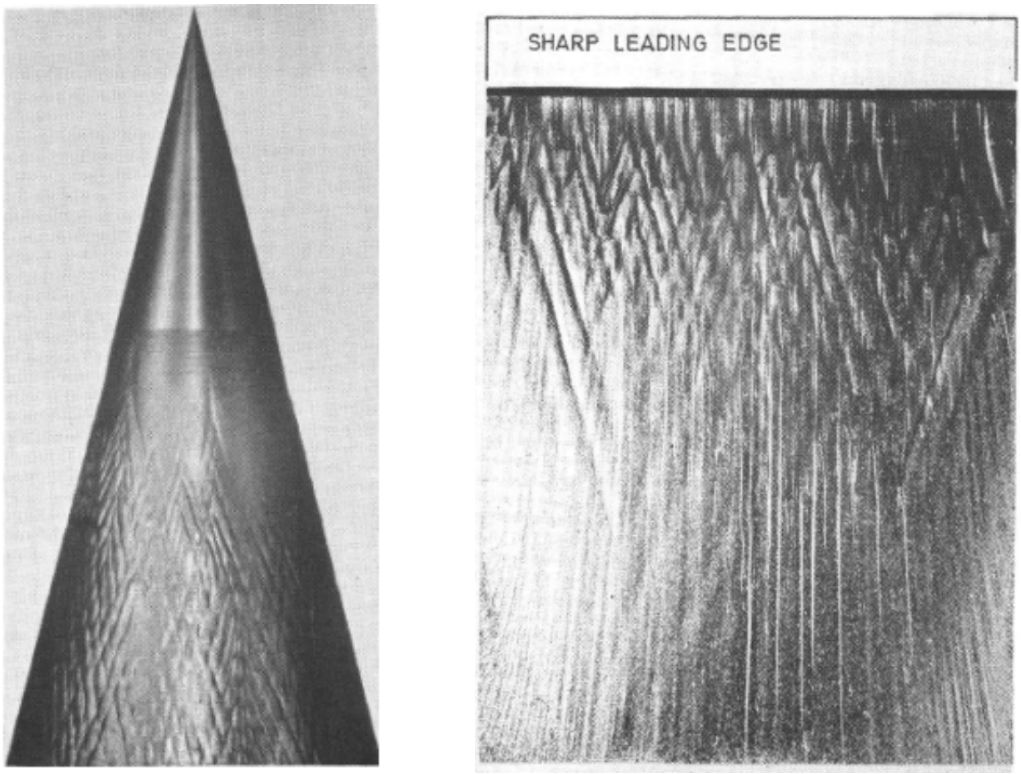

(a) 13^0 half cone Stock Cone (b) 10^0 Stock Flat Plate

Figure 6.1: Stock Models [15]

6.2 Computational Mesh

The computational mesh built for the simulations was constructed in Pointwise and built such that the boundary layers were fully resolved. Both models have split wall domains for specifying different boundary conditions for steel and camphor. Only half of the three-dimensional cone and a portion of the flat plate was simulated to save computational time and cost. The flat plate mesh also contains a ramp at the end of the domain that is not physical on the model. The expansion ramp is necessary to impose a supersonic boundary outlet condition correctly. Figure 6.2 illustrates the computational mesh and boundary conditions imposed. The metrics for both computational meshes are provided in Tables 6.2-6.3 and a grid sensitivity study was only performed on the flat plate simulation, as the cone simulation was a proof of concept.

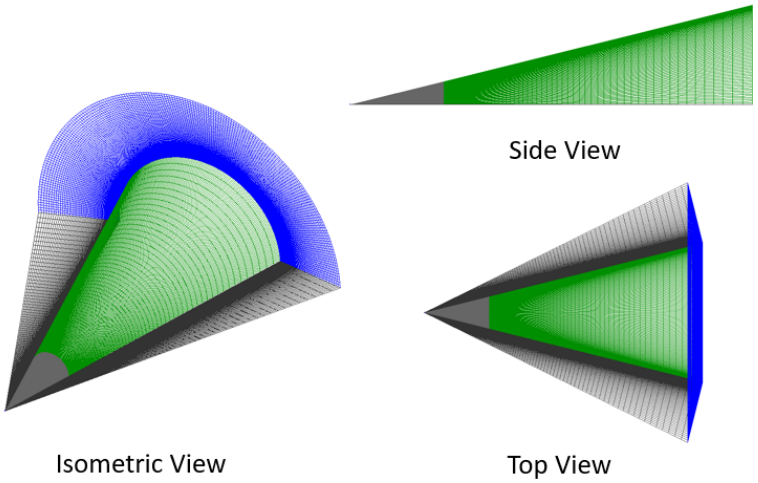

(a) 13^0 half cone Stock Cone

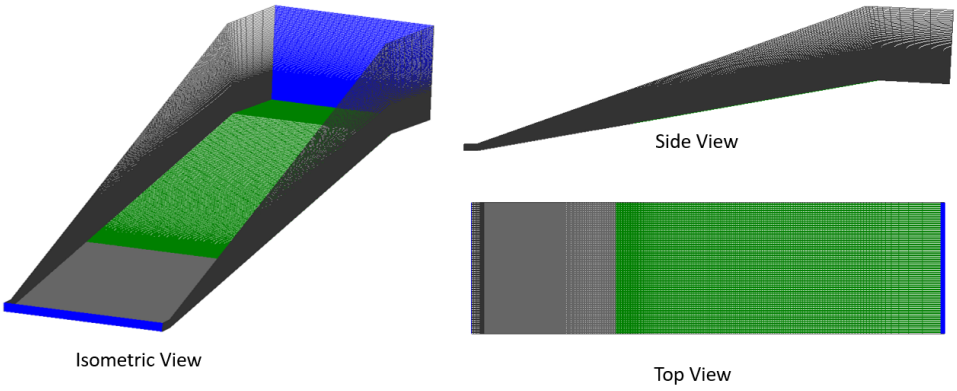

(b) 10^0 Stock Flat Plate

Figure 6.2: Computational Mesh with colored boundary conditions for illustration: Steel(grey), Camphor(green), Symmetry(black), Inflow and Outflow(blue)

Volume Mesh	Surface Mesh	Wall Normal Points	Wall Spacing (μm)
12,800,000	64,000	200	0.95

Table 6.2: Cone Grid Metrics

Volume Mesh	Surface Mesh	Wall Normal Points	Wall Spacing (μm)
17,871,400	89,357	200	0.95

Table 6.3: Flat Plate Grid Metrics

6.2.1 Steel Roughness

An addition of roughness was added to the computational mesh for the flat plate to provide forcing of disturbances. The roughness type chosen was a sandpaper type randomly distributed roughness and is more characteristic of a machined surface possibly seen in the experiments. A similar implementation of sandpaper roughness is shown in Dinzl and Gronval[54, 55]. The sandpaper roughness height chosen was a maximum of 1 micron applied to the plate's steel portion while the camphor portion was left smooth. The sandpaper surface roughness heights are applied to the geometry by sampling from a uniform distribution. Figure 6.3 illustrates the distribution of and heatmap of the roughness used in the simulation, followed by a close image of the steel-camphor junction on the flat plate.

6.3 Simulation Approach

Each simulation had a different numerical approach to understand how the ablation process can generate different surface patterns. The cone simulation is a steady-state calculation of turbulent numerical trips, while a flat plate is a DNS calculation with a rough leading edge. Both simulations were fruitful to illustrate how the sublimation process generates patterns on the camphor models and could lead to crosshatching patterns.

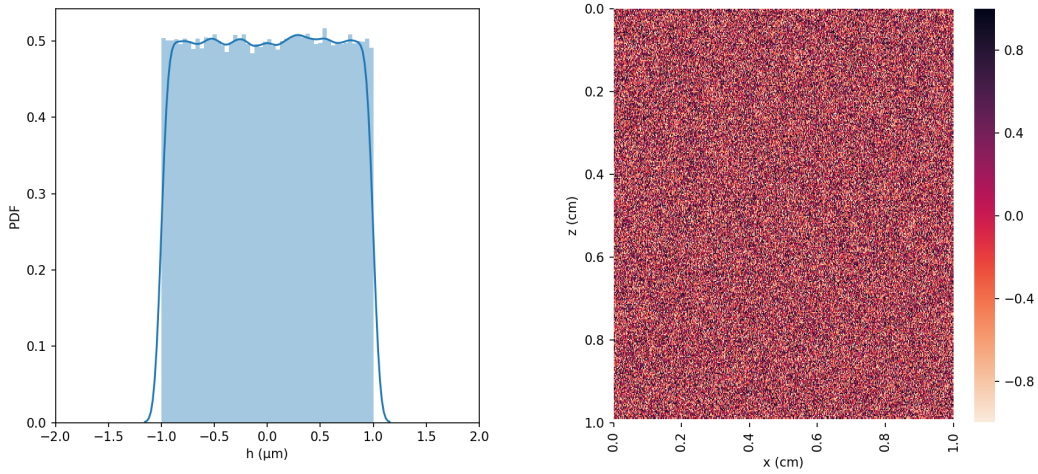

(a) Surface Perturbation Distribution (b) Surface Perturbation Heatmap

Figure 6.3: Steel Sandpaper Distributed Roughness

6.3.1 Cone Simulation

The steady-state cone had a numerical trip on the camphor surface 10cm downstream of the smooth steel-tip leading-edge which activates the SA model at the trip location, resulting in a turbulent wedge. The initial flow field with the numerical trip is converged with an isothermal wall boundary condition using Modified Steger Warming and an implicit time integration scheme. Once the baseflow is converged, the ablation boundary condition is imposed, which solves the species composition, sublimation rate, and temperature at the wall. The solid solver then solves the conduction through the wall for a user-specified conduction time with a new prescribed surface temperature, bringing the simulation forward in time. The solid span length prescribed reflects how long it will take for the material to respond to the fluid. For this problem, a small span of 10ms was chosen, which is conservative and reduces some heating lag but not all. After the solid has incremented, both the solid and fluid mesh move to account for the sublimation of camphor. The new shape changes the gas-mixture boundary layer state, and the fluid solver then solves several flow times to adjust to the changes. The implicit

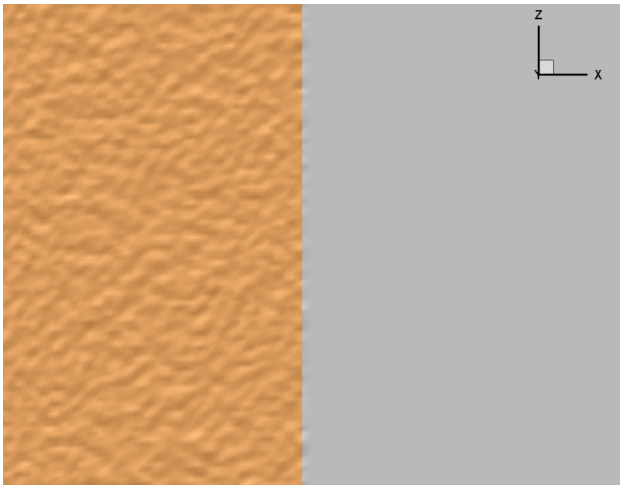

Figure 6.4: Steel-Camphor junction with surface roughness emphasized for illustration.

time integration method allows for significant time steps, and only a few hundred iterations are required to re-converge the boundary layer. The fluid-solid solver sequencing continues to repeat until a desired run time is complete.

6.3.2 Flat Plate Simulation

The baseflow for the flat plate fluid simulation was initially converged with an adiabatic wall using KSC higher-order low dissipation numerics. The rough-steel leading-edge generated unsteady streamwise vortices causing the simulation to become very stiff. For this simulation, the solid mesh was omitted, and the conduction through the solid was ignored. Neglecting the conduction through the wall is appropriate for this simulation due to the physical run time and the properties of camphor as a poor conductor. Previous numerical experiments that included the solid also justified this assumption. Once the baseflow is converged, the camphor boundary condition is imposed to solve for new wall properties. Due to the unsteady behavior, a fully coupled solution was required, and the grid is moved after every fluid time step. At this high Reynolds number condition, there was a time-step restriction to keep the solution stable, limiting the physical time for the simulation duration. The fluid time step for this simulation was a nanosecond, and because the time step was small, a factor was applied to the surface recession speed. The factor was only applied to the recession rate and did not affect the

conservation of mass or energy. A factor of 10^4 was chosen for the simulations, which was a tiny fraction of the surface friction velocity. Without the wall recession factor, it would be impossible to simulate the time required for the surface patterns to appear in the experiments (on the order of decades). Figure 6.5 is an example of the shear friction velocity, the recession velocity with and without the factor along the center of the plate in the axial direction for the flat plate conditions. The wall at these conditions is moving very slowly compared to the speed of the flow and should not impact the solution.

A grid sensitivity was performed for this simulation to ensure the proper resolution of unsteady disturbances. A refined mesh was generated with points in the axial and spanwise direction doubled compared to the baseline grid while the wall-normal cell count and first wall spacing were left unchanged. The recession distance for both simulation is plotted in Figure 6.6b. The length scales of the recession due to the streamwise vortices are similar for both the refined and baseline grid illustrating that the flow is selecting instabilities that are not driven by the sandpaper roughness imposed.

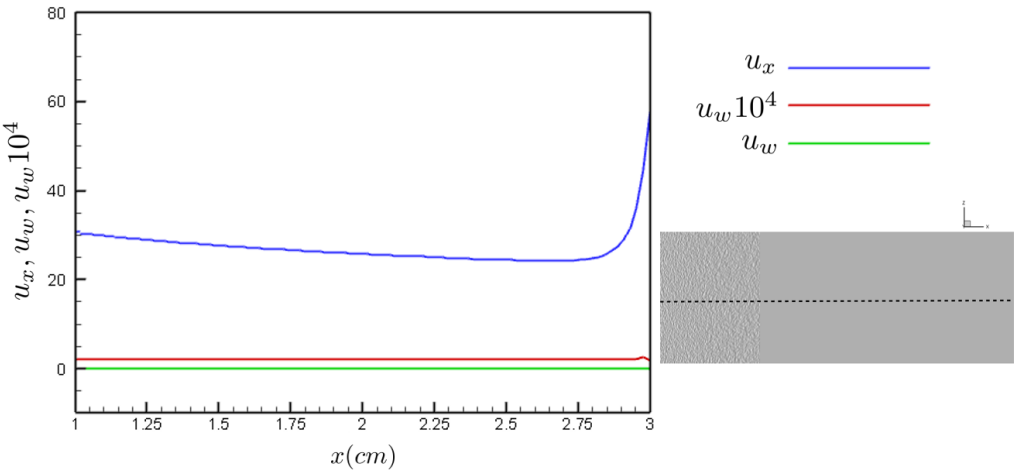

Figure 6.5: Surface Friction Velocity, Recession Velocity, Recession Velocity*Factor

Grid	Volume Mesh	Surface Mesh	Wall Normal Points
Baseline	17,871,400	89,357	200
Refined	72,315,000	361,575	200

Table 6.4: Flat Plate Grid Sensitivity Metrics

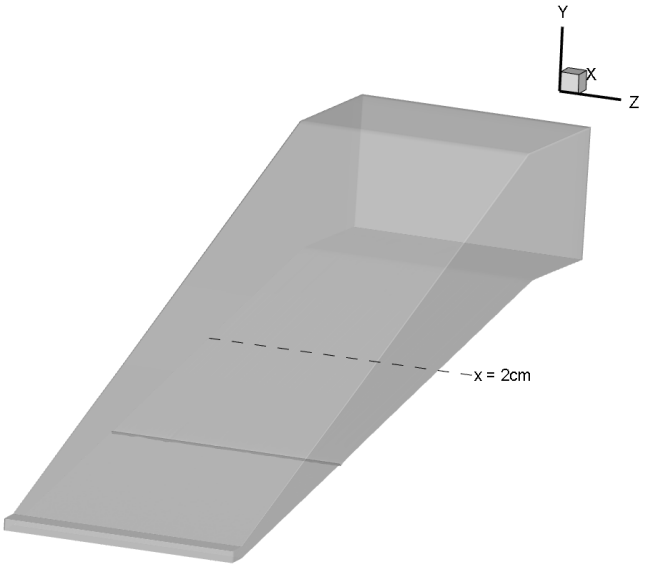

(a) Data Extraction Location

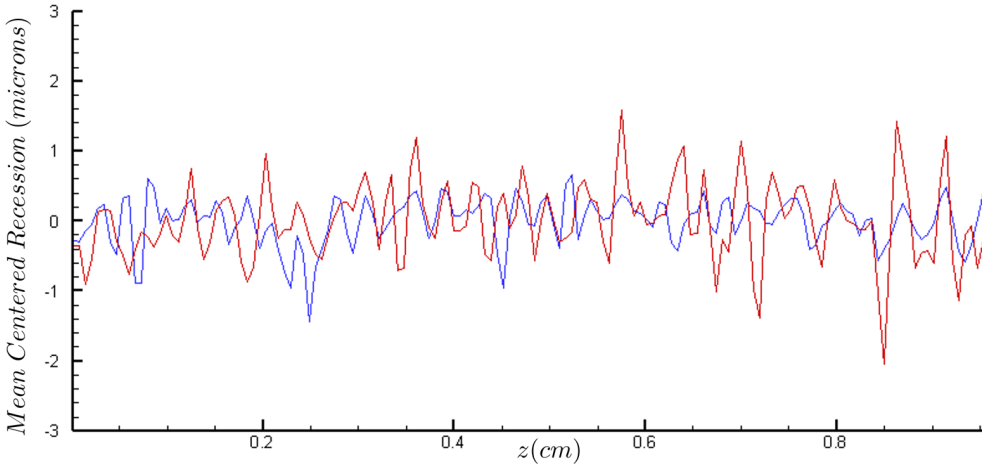

(b) Spanwise Recession Red(Refined) Blue(Baseline)

Figure 6.6: Grid Sensitivity to Recession

Chapter 7

Numerical Results

7.1 Ablation Wedge on a Cone

An ablation wedge on a cone was simulated with a steady-state approach similar to the validation simulation. The initial flow field without ablation is shown in Figure 7.1. Mach contours are plotted on the symmetry planes, and surface heat flux is plotted on the cone surface. For the initial conditions, a cold isothermal wall was converged before starting the ablation process. Notice the higher heating and turbulent wedge generated by the numerical trip. The wedge angle is noted to be smaller than experiments and discussed further by Spalart [56]. Nevertheless, this simulation's goal is not to capture the wedge angle but to show the capability to run turbulent simulations with the ablation code and understand how the ablation process in a laminar-turbulent simulation could trigger crosshatching patterns.

The advantage of running the simulations with Steger-Warming with DPLR is the ability to take significant time steps. The simulation can progress comparable to the wind tunnel run times. Figure 7.2 is the temporal progression up to 20 seconds, and the recession distance is on greyscale where lighter grey is a smooth surface, and darker grey corresponds to a deeper recession. At the start of the simulation, the cone is essentially smooth, and as the simulation progresses and camphor begins to sublimate, forming an ablation wedge. At the end of the simulation, the recession depth shows very localized grooves forming on the edges of the turbulent cone.

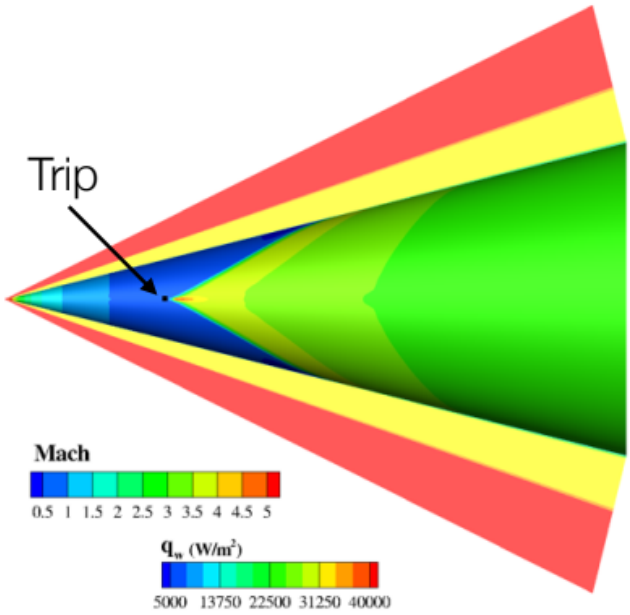

Figure 7.1: Turbulent Wedge Cone Baseflow Simulation Mach and Surface Heat Flux Contours

The mass flux of camphor and wall temperature contours are plotted in Figure 7.3 at 20 seconds. As expected, the wall temperature and camphor mass flux are lower in the laminar region than in the turbulent area. Once the flow turns fully turbulent, there is a spike in temperature and camphor in the boundary layer. A line data exaction on the surface in the axial direction illustrates the jump in temperature, mass flux, and recession distance in Figure 7.4 exhibiting the local groove development. These localized grooves could potentially lead to an understanding of how crosshatching begins to form. In the literature, experimentalists who observed ablation wedges noted that the crosshatching patterns were created inside the wedge. A possible mechanism is that the localized grooves may be generating weak acoustic waves in the supersonic boundary layer, initiating the diamond-shaped patterns.

A simple numerical experiment was conducted with a two-dimensional model highlighting how large temperature gradients form grooves. For this simulation, a cold wall

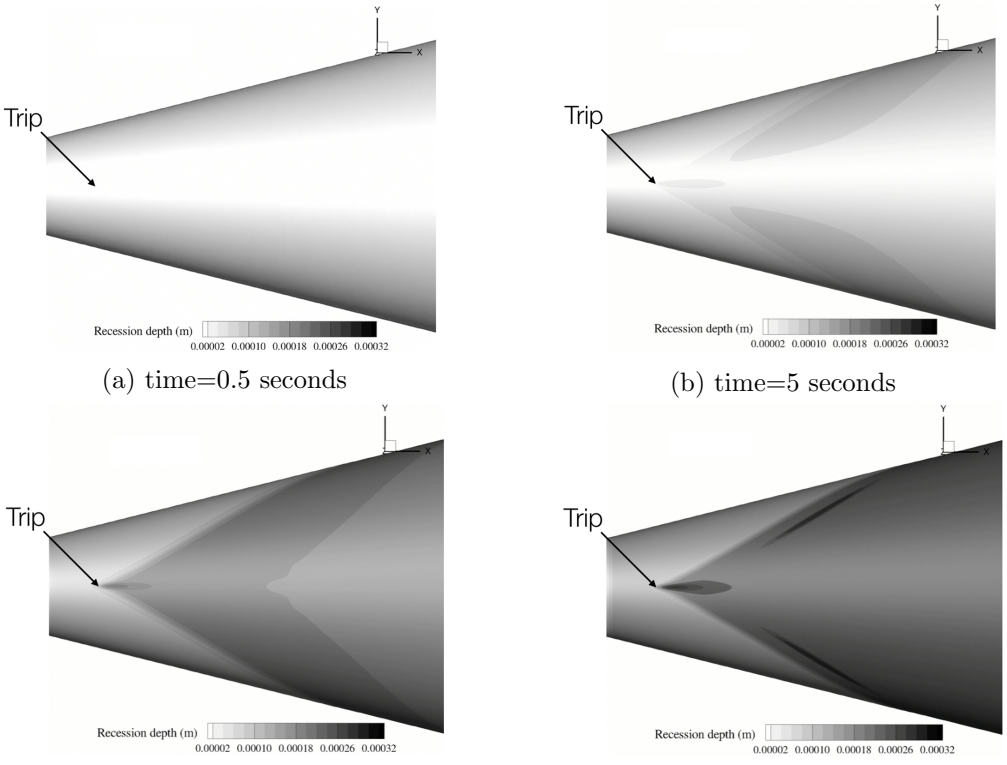

(a) time=0.5 seconds (b) time=5 seconds

(c) time=15 seconds (d) time=20 seconds

Figure 7.2: Turbulent Wedge Cone Simulation: Temporal Progression of Surface Recession

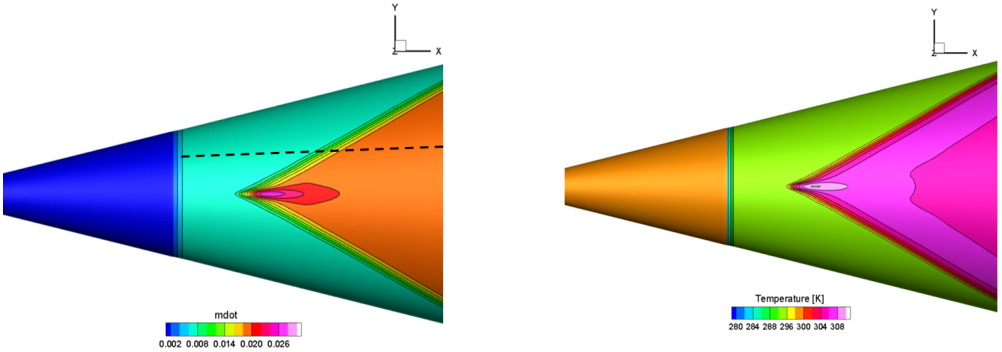

(a) Camphor Mass Flux Contours (b) Wall Temperature Contours

Figure 7.3: Turbulent Wedge Cone Simulation: Temperature and Mass Flux of Camphor at time=20 seconds

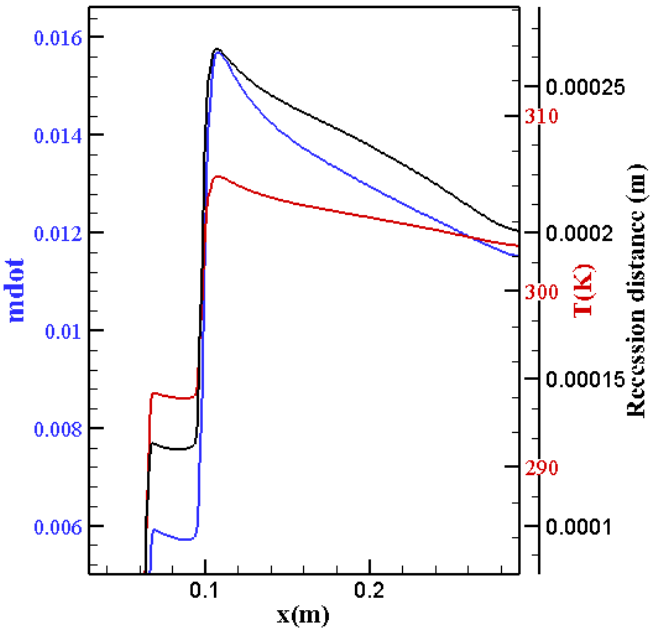

Figure 7.4: Mdot, Temperature and recession axial variation across turbulent wedge

set to T=250K followed by a hot wall set to T=320K. Referring back to Equation 4.36 and Equation 4.37 the mass flux equation for camphor is inversely proportional to the square root of wall temperature and the difference between the vapor pressure and partial pressure of camphor. The vapor pressure of camphor also grows exponentially with wall temperature. After running the ablation code, wall properties are plotted in Figure 7.5b and show the vapor pressure of camphor and mass flux jump due to the large temperature gradient. A local peak in the difference between the vapor pressure and partial pressure of camphor persists, leading to a higher mass flux of camphor and consequentially formation of grooves.

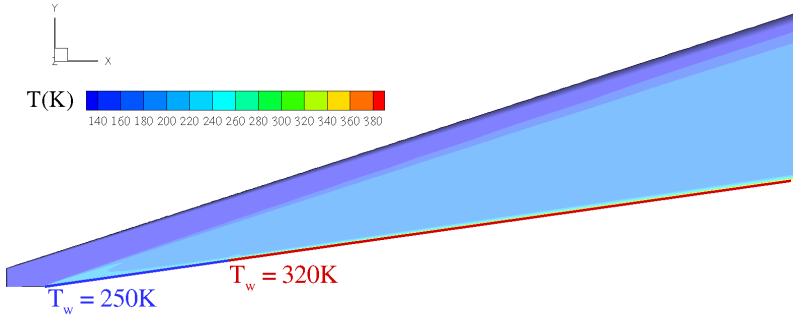

(a) Temperature Flowfield Contours

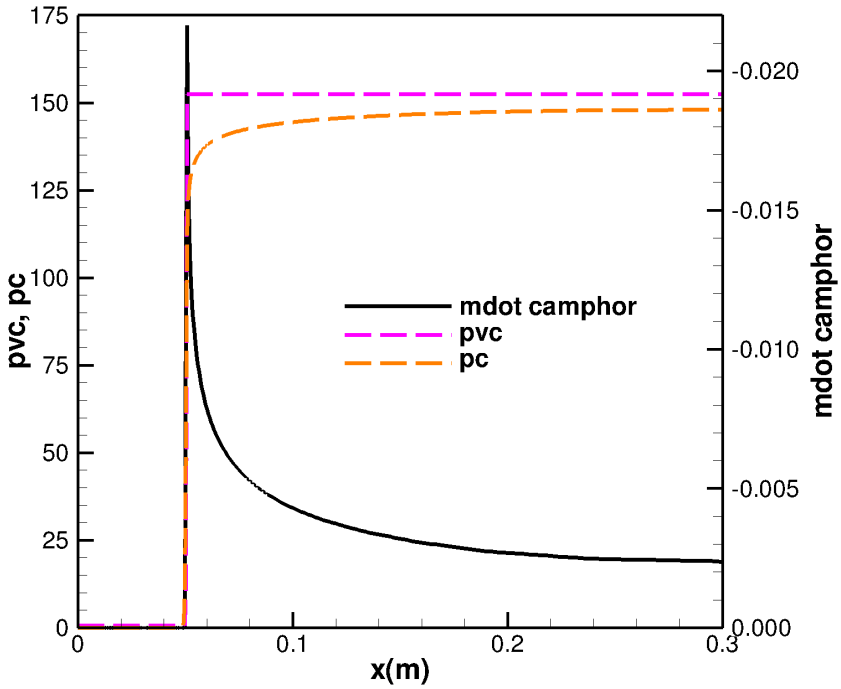

(b) Wall Properties

Figure 7.5: Two-Dimensional Simulation with Large Temperature Gradient

7.2 Streamwise Vortices On a Flat Plate

A DNS simulation was performed on a flat plate at a 10-degree angle of attack, similar to the Stock flat plate experiment. Due to the high Reynolds number and the computational cost to run the ablation simulations, only a portion of the domain is calculated. Figure 7.6 outlines the computational domain in red. The domain is large enough in the spanwise direction to capture several streamwise vortices and long enough in the streamwise direction to capture their effect.

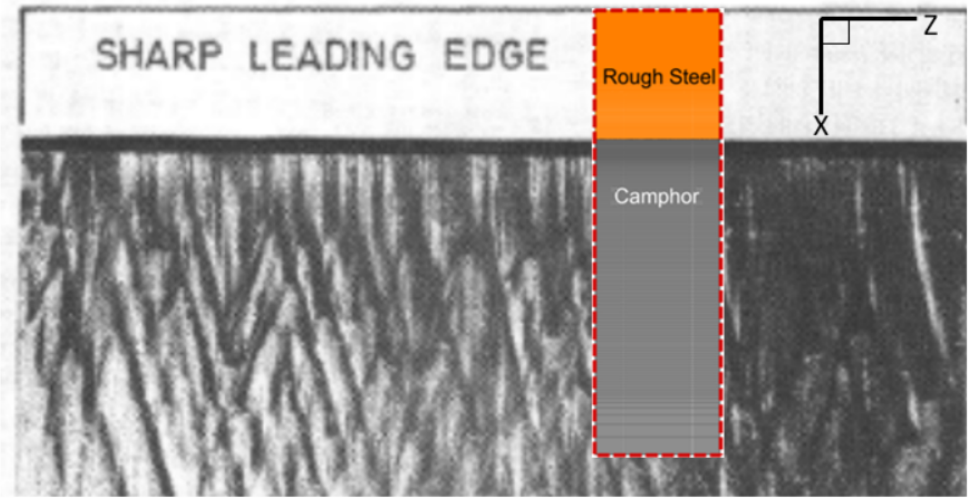

Figure 7.6: DNS Computational Domain of Stock 10^o plate Outlined

7.2.1 Baseline

The baseline simulation is at the conditions of the Stock flat plate where crosshatching was observed. Notice, in Figure 7.7 there is evidence of streamwise vortices etching narrow grooves downstream of the camphor-steel interface. It was common for an experimentalist to observe streamwise vortices in the vicinity of crosshatching patterns; therefore, it was postulated that the vortices could contribute to the initiation of the diamond-shaped patterns. One method to generate streamwise vortices in CFD is to introduce surface roughness. For these simulations, a sandpaper roughness was imposed on the non-ablative steel portion of the flat plate. As the ablation begins and

a backward-face develops, the shear layer generated by the step acts as an amplifier for the streamwise vortices. Figure 7.8 are images of the flowfield for the baseline simulations. The camphor molecular weight is significantly higher than air; thus, most camphor species stay close to the surface. Figure 7.8b illustrates the thin camphor layer and the separation bubble caused by the steel-camphor interface. The results presented here and further exclude the rough steel plate from the plots, and the flow is moving in the positive x-direction from top to bottom.

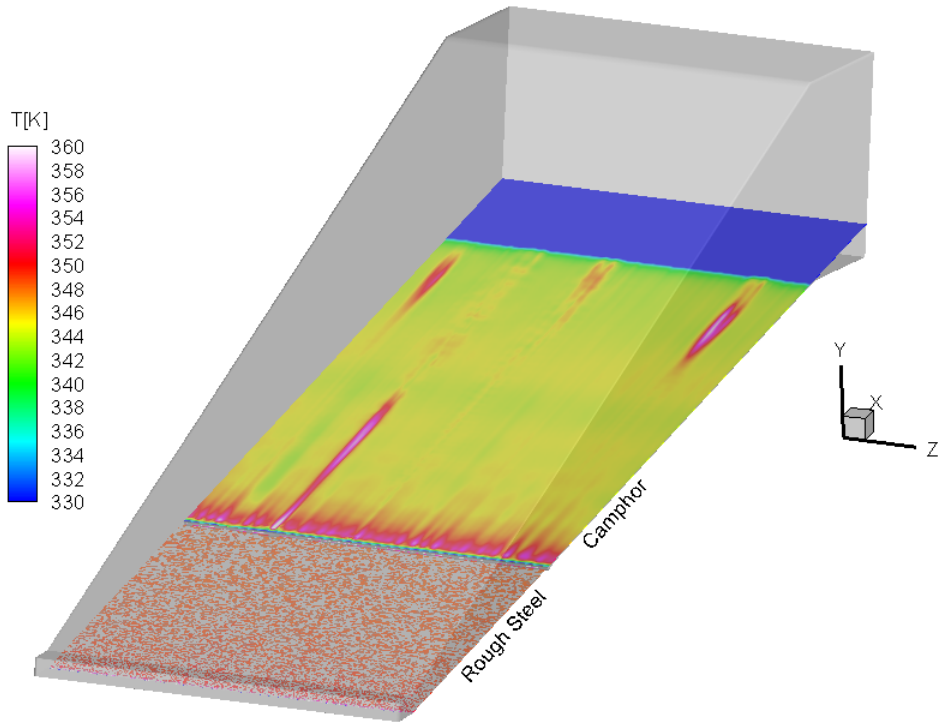

Figure 7.7: Streamwise Streaks due to Streamwise Vortices

Figure 7.9 is a temporal progression of temperature, mass flux, and camphor mass fraction for up to 24 flow times. At 16 flow times, the backward-facing step is starting to develop, as shown in the higher temperature located at the top of Figure 7.9a. Turbulent spots are developing downstream, and a small amount of camphor is sublimating. A few flow times later, temperature streaks develop due to the streamwise vortices, and more camphor is introduced into the boundary layer but not a significant amount. The

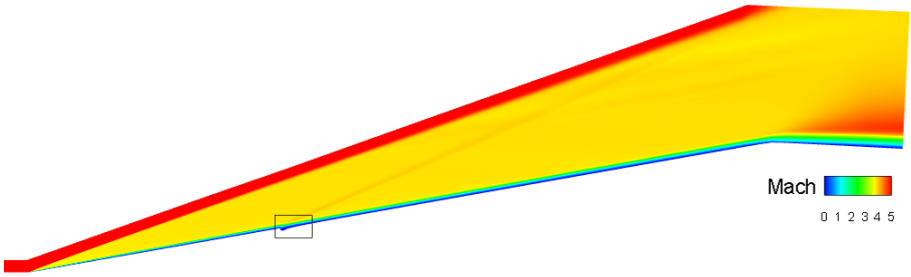

(a) Mach Contours

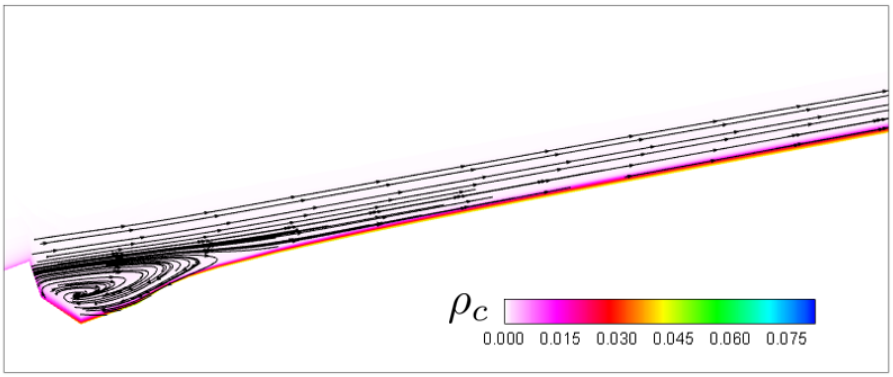

(b) Camphor Density

Figure 7.8: Baseline Flow of Stock 10^o Plate

introduction of camphor species into the boundary layer seems to stabilize even at small mass fractions. At 21 flow times, the turbulent spots have vanished, but now the groove is deepening at the steel-camphor interface, and the streaks again start to form, and turbulent spots arise at the final stage of the simulation. The flow will continue to follow this pattern. The vortices are amplified due to the deepening of the backward-facing step and grow downstream, creating turbulent spots. Narrow grooves etched into the surface due to vortex interaction with the surface increase the sublimation rate. The addition of camphor gas into the boundary layer then stabilizes the boundary layer, and the process repeats itself as the backward-facing step grows.

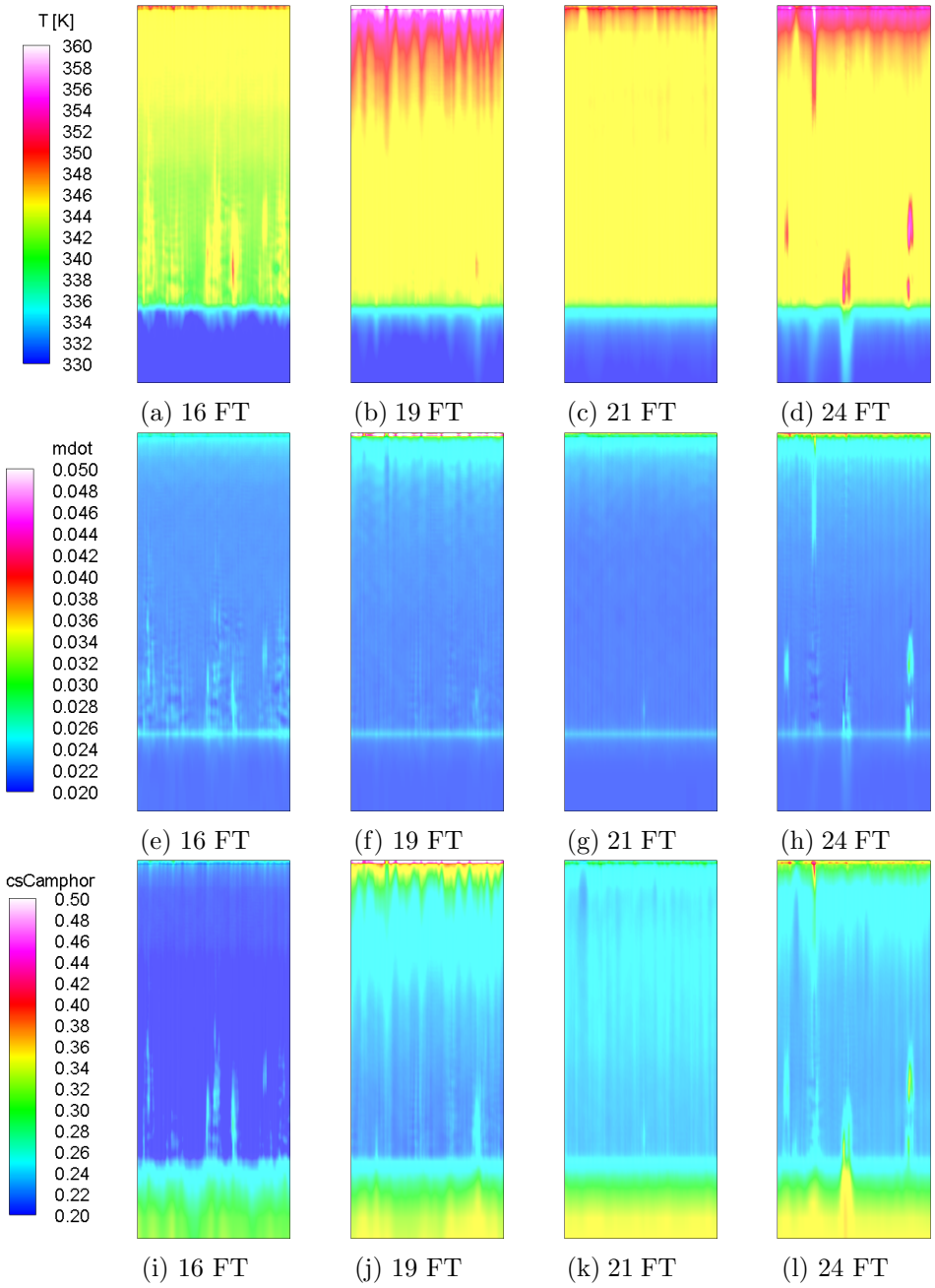

(a) 16 FT (b) 19 FT (c) 21 FT (d) 24 FT

(e) 16 FT (f) 19 FT (g) 21 FT (h) 24 FT

(i) 16 FT (j) 19 FT (k) 21 FT (l) 24 FT

Figure 7.9: Flow Time (FT) Progression of Wall Temperature (top row), Camphor Mass Flux (middle row), and Camphor Mass Fraction (bottom row).

7.2.2 Reynolds Number Effects

A Reynolds number sensitivity study was performed to understand the effects on flow behavior and pattern development. The flat plate camphor model was simulated at a low, medium (baseline), and high Reynolds number. The freestream conditions are provided in Table 7.1. This study was also motivated by the most recent crosshatching work of Pu Qun, who conducted an experimental study on a sphere cone to understand the evolution of crosshatching patterns [16]. In his work, he noticed different surface patterns formed at a range of Reynolds numbers. Figure 2.6 shows patterns he observed at different Mach number and stagnation pressure combinations. The dotted lines are iso-lines of Reynolds number based on boundary layer properties. For a constant Mach number at the lowest Reynolds number condition, the surface maintained a smooth surface. As the stagnation pressure increased, other patterns started to form, including narrow grooves, pits, ablation wedges, crosshatching, and regmaglypts. Similar patterns fall along the same iso-Reynolds line indicate a strong relationship between pattern type and Reynolds number. The observations of this study are consistent with the literature that a moderate Reynolds number is required for the formation of surface patterns.

Simulation –	Mach –	T [K]	ρ [kg/m^3]	Re [1/m]
Low Re	5.3	60	0.116	24 Million
Baseline Re	5.3	60	0.232	48 Million
High Re	5.3	60	0.349	72 Million

Table 7.1: Reynolds Sensitivity Study Freestream Conditions

Initial observations of the flowfield at different Reynolds numbers show the low Reynolds number is laminar, the baseline is transitional, and the highest Reynolds number is fully turbulent. Figure 7.10 illustrates the effects of laminar-turbulent transition on wall temperature and camphor mass fraction at 17 flow times. At all three Reynolds numbers, there is a presence of streamwise streaks. For the lower Reynolds number, the streaks are smooth for the length of the simulation with no signs of transition or turbulence. Turbulent spots start to form at the baseline conditions, and finally, at the highest Reynolds number, the flow is fully turbulent.

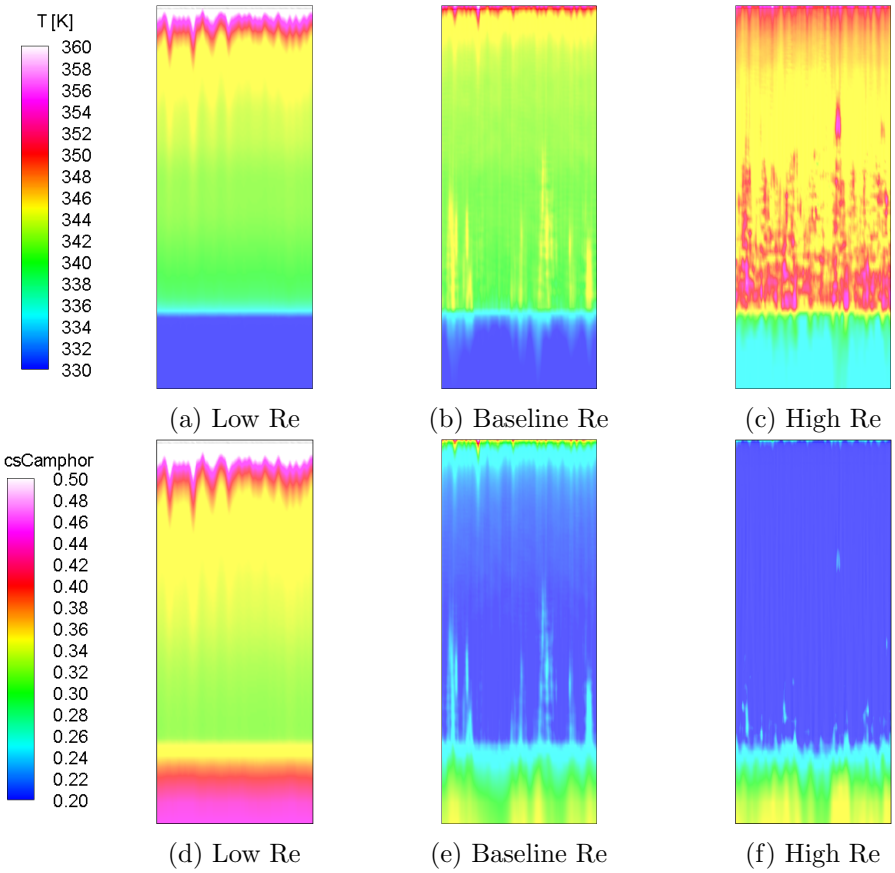

(a) Low Re (b) Baseline Re (c) High Re

(d) Low Re (e) Baseline Re (f) High Re

Figure 7.10: 17 Flow Time Comparison of Low, Baseline and High Reynolds Number Simulations

Localized heating is higher at the steel-camphor junction and a higher mass fraction of camphor in the boundary layer at the lower laminar Reynolds number condition. At first, this seems counter-intuitive to have a higher wall temperature for the lower Reynolds number. As mentioned previously, the sublimation of camphor is driven by the difference between the camphor vapor pressure and partial pressure $\dot{m} \approx (p_{vc} - p_c)$. The near-wall density is lower at the lower Reynolds number condition, which translates to the lower partial pressure of camphor and higher mass flux, creating a deeper backward-facing step. The deeper grooves will cause higher localized heating resulting in a spike in temperature. The highest Reynolds number condition has the opposite effect at the camphor-steel junction generating a shallower groove. Figure 7.11 is a side view

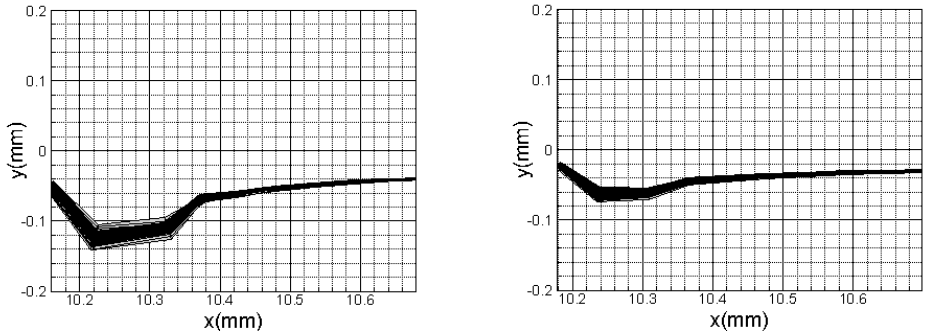

(a) Low Re (b) High Re

Figure 7.11: Side View of Surface Recession at the Steel-Camphor Junction

of the surface recession at the steel-camphor junction for both high and low Reynolds numbers. Notice, the low Reynolds number condition step depth is about double the higher Reynolds number condition. The increased recession for the lower Reynolds number condition adds to the stability of the boundary layer. As the flow progresses downstream for all three Reynolds numbers, the temperature of the camphor surface rises significantly as the Reynolds number is increased. The variation in temperature rise is due to the laminar and turbulent flow characteristics. The heat transfer rates are much larger for turbulent flows than those of laminar flows because the turbulent fluctuations increase heat and momentum transfer between fluid particles. Temporal progression of temperature, camphor mass fraction, and camphor mass flux for all simulations are provided in Appendix A.

In Qun's experiments, he showed a progression of pattern development with increasing Reynolds numbers from smooth surfaces to narrow grooves at moderate Reynolds numbers. For the flat plate simulations, a similar progression was also observed. Figure 7.12 is a plot of recession depth measured from the initial pre-ablated surface. The light or white contours show low recession depth, while dark or black contours show more considerable recession depth. For all three cases, the backward-facing step and recirculation zone are present, but further downstream, the characteristics of the surface are different. The lowest Reynolds number condition has a smooth surface, and in contrast, the highest Reynolds number condition exhibits narrow grooves consistent with the observations found in the sphere cone experiments.

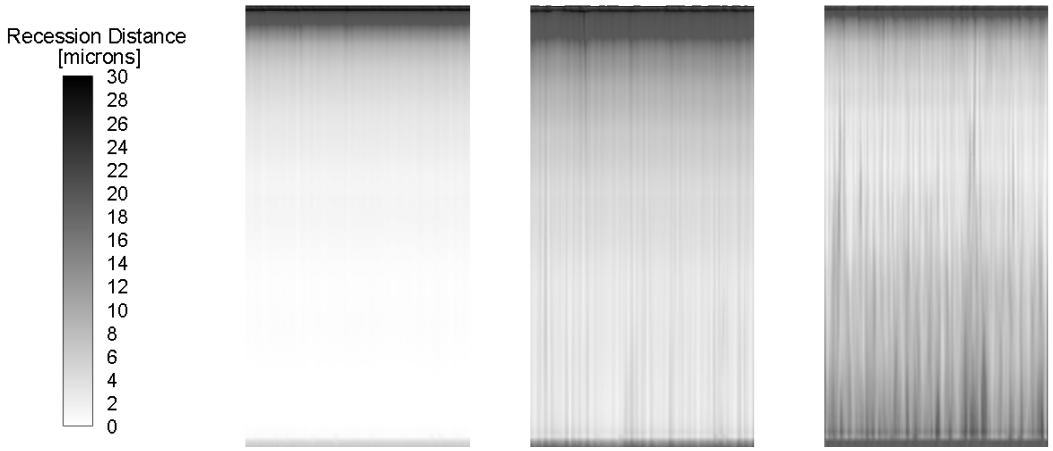

(a) Low Re (b) Baseline Re (c) High Re

Figure 7.12: Recession Depth

A line extract at x=2.5cm of recession depth for each of the simulations is shown in Figure 7.13. Notice the grey line, which is the lowest Reynolds number, is essentially smooth, while the spanwise variation in recession depth and the groove depth grows as Reynolds number is increasing.

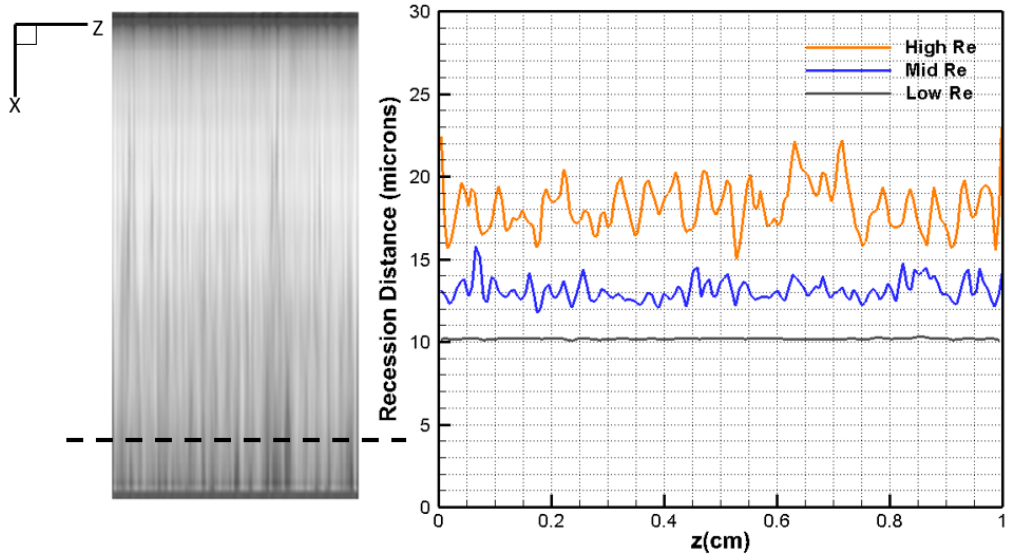

Figure 7.13: Recession Depth at x=2.5cm

7.2.3 Surface Motion

A sensitivity study was performed to understand how the surface motion impacts the flow patterns and transition development. For this study, the baseline Reynolds number is used for both the static mesh and the moving mesh. The critical feature that develops in the moving mesh that is not created in the static mesh is the backward-facing step between the steel and the camphor slap and, consequently, forming a small recirculation bubble. Figure 7.14 is the temporal temperature progression comparing the static mesh to the moving mesh at several flow times. As time progresses, the streamwise streaks begin to form on the surface for the moving mesh but are absent in the static grid. The flow also reveals more turbulent areas for the static mesh initially absent for the moving mesh. The striations for the moving mesh simulation cause a higher heat load on the camphor surface which manifests to a higher sublimation rate than the non-moving mesh. Figure 7.15 is the temporal progression of mass fraction of camphor. The mass fractions are the same at the beginning of the simulation, but substantially more camphor is in the moving mesh boundary layer as the simulation progresses. Downstream of the backward-facing step, there is a localized increase in camphor mass fraction compared to the non-moving mesh. The turbulent spots also appear for both simulations but are delayed for the plate with a backward-facing step. The presence of the camphor in the boundary layer delays and moves the transition region downstream, which emphasizes the stability effect of the camphor species.

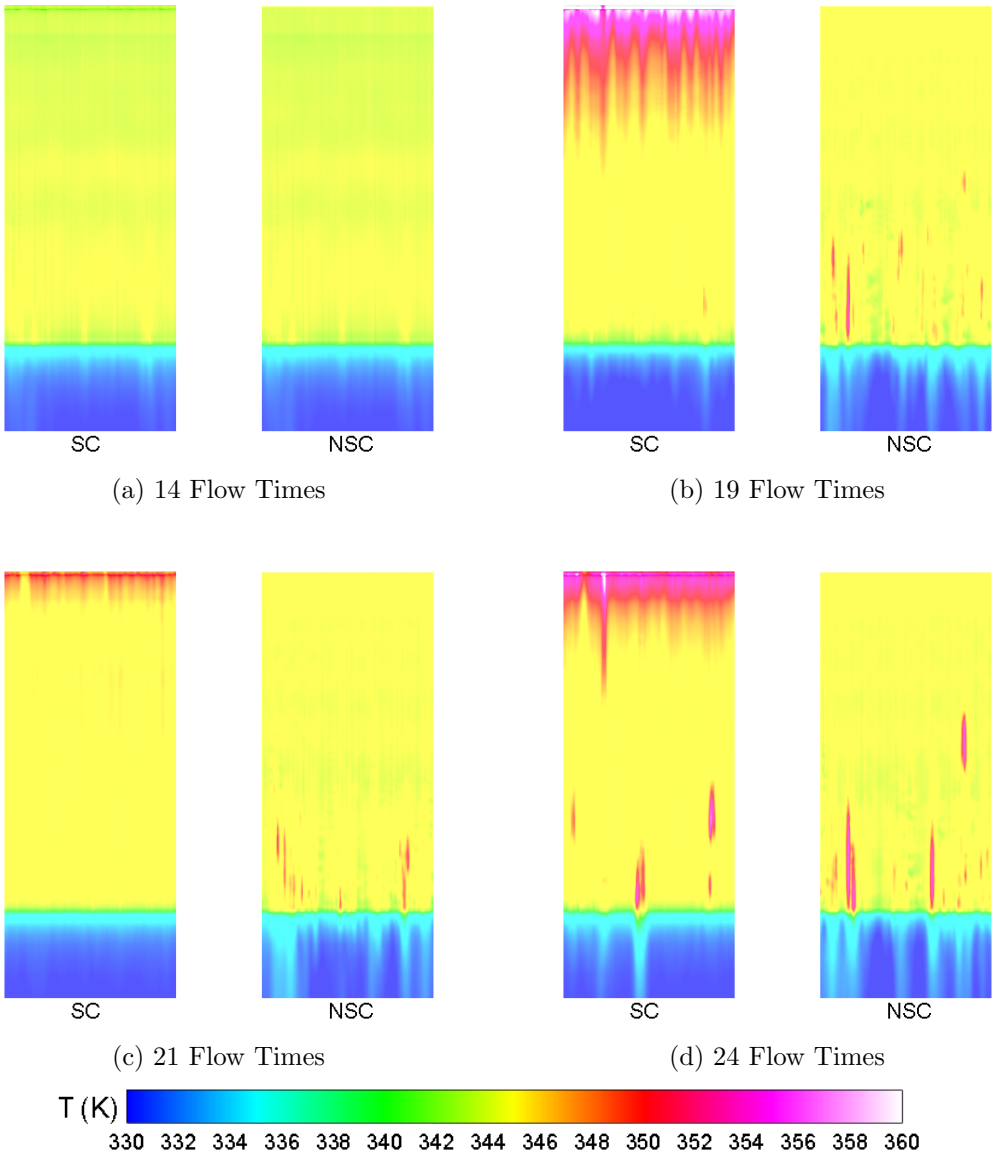

(a) 14 Flow Times

(b) 19 Flow Times

(c) 21 Flow Times

(d) 24 Flow Times

Figure 7.14: Temporal Wall Temperature for Shape Change (SC) and No Shape Change (NSC) for Baseline Reynolds Number Simulations

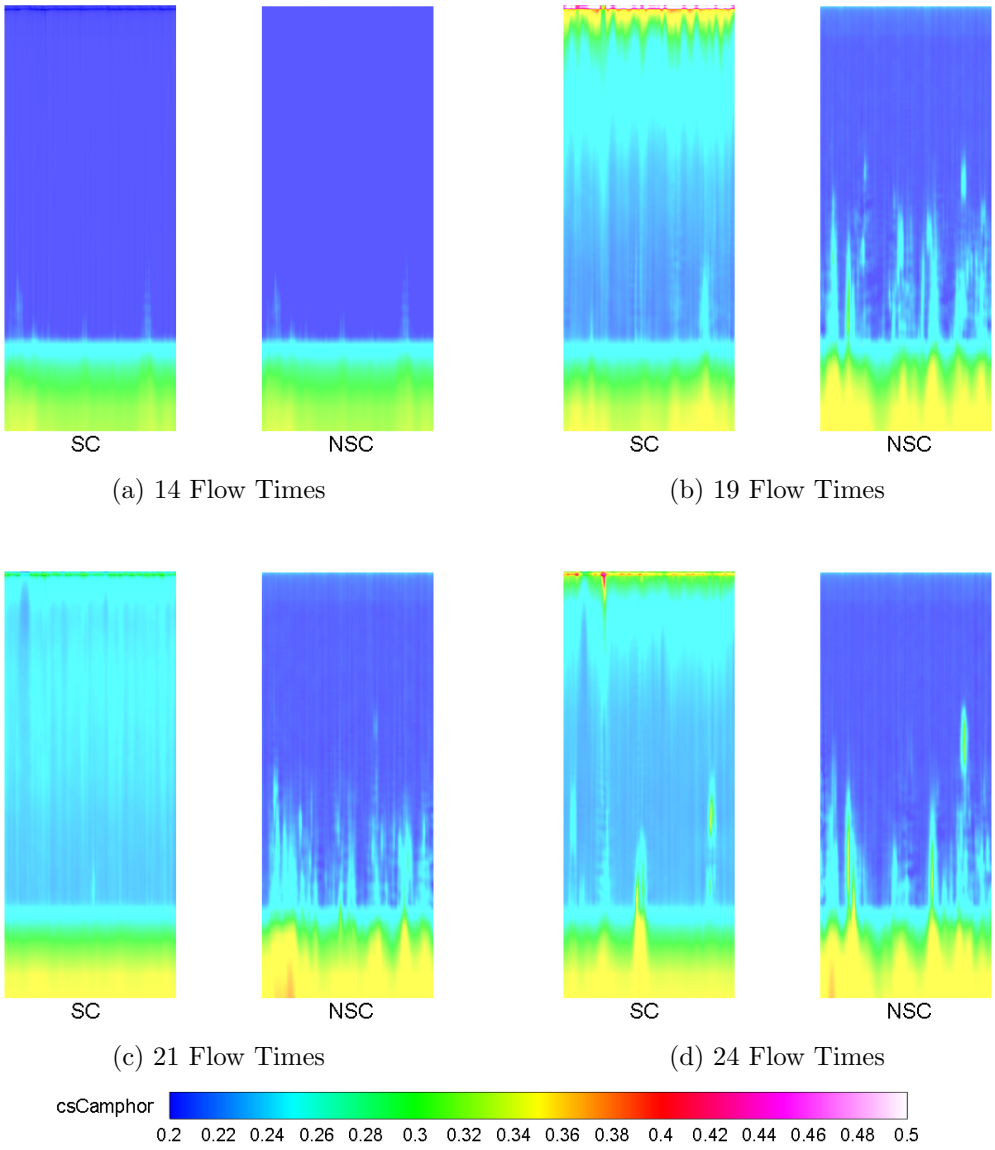

(a) 14 Flow Times

(b) 19 Flow Times

(c) 21 Flow Times

(d) 24 Flow Times

Figure 7.15: Temporal Mass Fraction of Camphor for Shape Change (SC) and No Shape Change (NSC) for Baseline Reynolds Number Simulations

7.2.4 Camphor Boundary Layer

A numerical study comparing the baseline simulation to an adiabatic wall without ablation is used to emphasize the camphor gas effect in the boundary layer. Gaponov

and Smorosky using linear stability analysis, showed that injecting a foreign gas significantly heavier than that of the primary gas into the near-wall sub-layer of the supersonic boundary layer has a stabilizing influence on the boundary layer [57, 58, 59]. The opposite occurs with the injection of a lighter molecular weight, which has a destabilizing effect. The cooling of the surface due to the sublimation process decreases the surface temperature, increasing the near-wall momentum, stabilizing the boundary layer. This effect does not occur in the adiabatic wall without ablation, where the temperatures are much higher. Figure 7.16 shows temporal temperature progression of the adiabatic wall transitioning to fully turbulent almost immediately at these flow conditions. Based on these results a heavy gas sublimation shows a potential mechanism to prevent or delay the transition to turbulence.

.

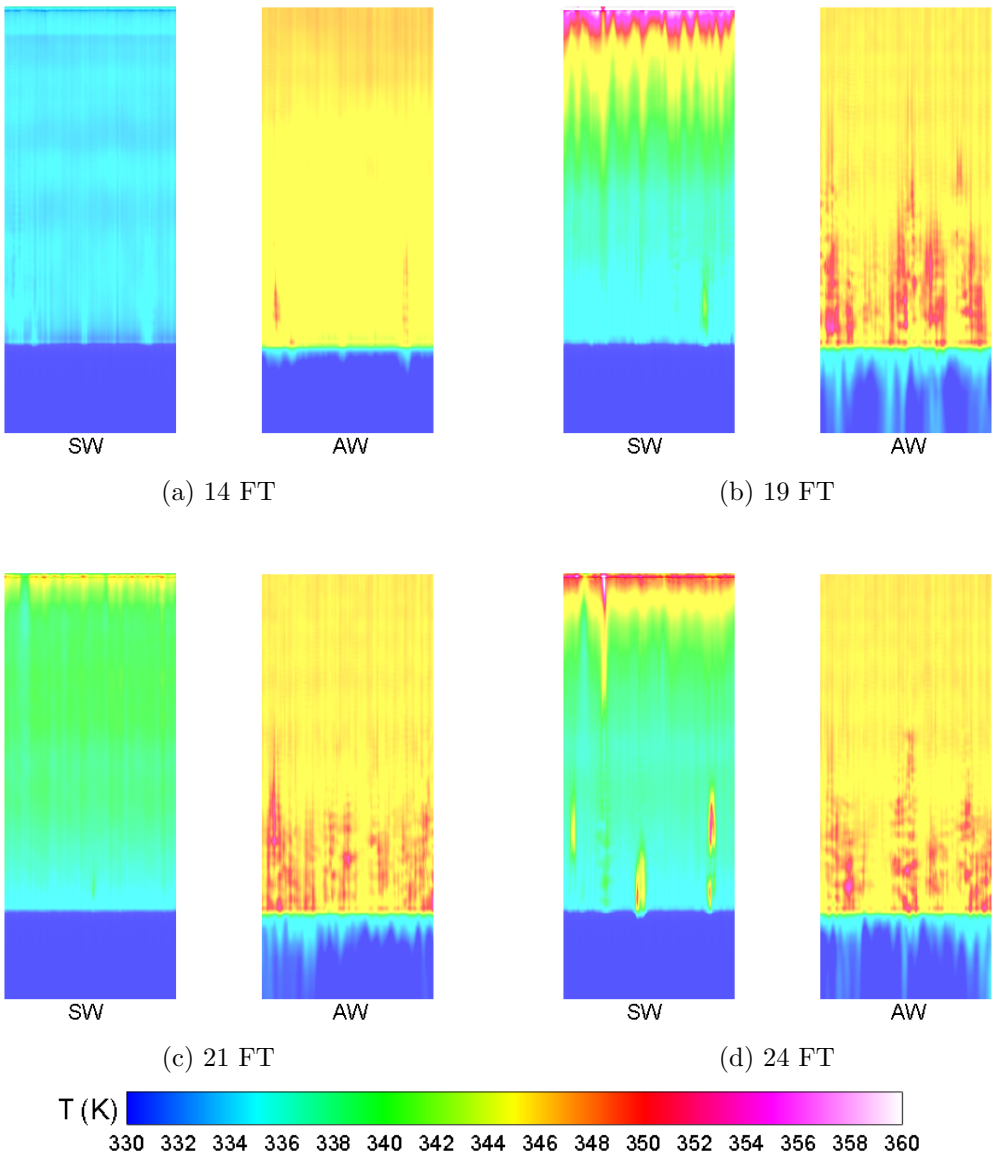

(a) 14 FT (b) 19 FT

(c) 21 FT (d) 24 FT

Figure 7.16: Flow Time (FT) Progression of Wall Temperature for Sublimating Wall (SW) and Adiabatic Wall (AW)

Chapter 8

Conclusions

This research aimed to understand the mechanisms that initiate crosshatching patterns on ablative materials in supersonic flow conditions for which the underlying mechanism is still not yet known. In the process of studying crosshatching, a contribution of this research implemented and validated a camphor sublimating boundary condition into the US3D fluid-solid solver with a moving mesh. Numerical studies were then performed at wind tunnel conditions where crosshatching was observed.

The numerical results are most consistent with Qun's observations of pattern development. For the flat plate baseline conditions where Stock observed crosshatching, very localized deep grooves started to form downstream of the steel-camphor interface. It's possible this groove, with enough time, would keep locally receding and potentially create a pit. The pit would become the apex of a Mach cone that would interact with the streamwise vortices, similar to the postulate by Tobak, and the patterns would form from the Mach cone and streamwise vortex interaction.

The ablation wedge cone simulation illustrated a similar effect: large temperature gradients translate to deep localized grooves due to the sublimation process. One agreement between experimentalists in the past was that transitional or turbulent flow was required for the onset of crosshatching. Transitional flows can exhibit large temperature spikes, which can result in localized deep grooves. The presence of camphor in the boundary layer for the baseline simulation created a stability effect delaying the transition spots and moving them downstream. The fluctuations in temperatures due to this process could expedite the pit formation further.

A path forward to understand more about pattern development is to simulate an imperfection on the camphor surface. No permeable surface is perfectly smooth, and perhaps an imperfection in the surface material accelerates the crosshatching initiation. A flat plate was the primary workhorse of this numerical study, but most of the experiments were tested on sphere-cones or cones. Both cones with and without steel tips exhibited crosshatching, and future work is required to understand how geometry affects the progression of pattern development. If crosshatching is eventually observed, there is enough literature for cones to compare simulated patterns with observed cant angles and wavelengths in experiments. Stock and Ginoux cone experiments at VKI are the most extensive crosshatching experimental data in the literature [1].

Nachtsheim and Larson studied how the surface material influenced the formation of crosshatching. They discovered that as the viscosity of the material increased, both the thickness of the melt and Reynolds number of the melt increased and suppressed pattern formation. Future work to simulate different viscosity materials would investigate Nachtsheim and Larson's work and understand the effect of material properties on pattern development.

It takes substantial time for crosshatching patterns to develop. Stock and Ginoux correlated the edge pressure of the boundary layer to the time required for pattern development. The higher the edge pressure, the shorter the run time required for pattern formation. Still, the run times required to observe crosshatching are in the order of seconds and not milliseconds. Simulation of the ablation process with DNS is complex due to the significant variation in time and spatial scales between the solid and the fluid. In order to recede the surface in a reasonable time, a recession rate factor that was much less than the local skin friction velocity was applied to speed up the camphor surface response. The speed-up factor might impact the solution tuning in to a different behavior if the factor was removed. A study to understand how the recession factor impacts the solution is required to understand this effect fully.

Another area for future work is additional improvements to the mesh deformation solver. Gidzak developed this code for deformable decelerator systems and not for models with adjacent ablative and non-ablative surfaces. The grid can eventually deform at the steel-camphor junction in a non-physical way, causing negative volumes in the mesh. This limitation was yet another restriction of available simulation time.

The few milliseconds of flow time simulated a very dynamic effect of the presence of camphor, the backward-facing step between the camphor and steel, and the streamwise vortices. Through the simulation sensitivity study of Reynolds number variation, static mesh motion, and fully adiabatic wall simulations, we now know that presence of camphor in the boundary layer is stabilizing. Another simulation to study the effect of camphor gas in the boundary layer is to run the backward-facing step meshes generated by the ablation process and run those geometries without ablation. It would be interesting to study if the stability characteristics change for this flow by removing the camphor species from the boundary layer and simulating the effect of the shear-layer generated by the ablation formed backward-facing step. Linear stability or I/O analysis is also another appropriate next step to understand the extent that camphor destabilizes or stabilizes the flow at these conditions.

References

[1] Hans W Stock and Jean J Ginoux. Hypersonic low temperature ablation an experimental study of cross-hatched surface patterns. In *Astronautical Research 1971*, pages 105–120. Springer, 1973.

[2] Andrew F Charwat. Exploratory studies on the sublimation of slender camphor and naphthalene models in a supersonic wind-tunnel. Technical report, RAND CORP SANTA MONICA CA, 1968.

[3] Carl L. Yaws. *Yaws' Handbook of Thermodynamic Properties for Hydrocarbons and Chemicals*. Knovel, 2009.

[4] Carl L. Yaws. *Yaws' Handbook of Thermodynamic Properties for Hydrocarbons and Chemicals*. Knovel, 2009.

[5] Carl L. Yaws. *Yaws' Transport Properties of Chemicals and Hydrocarbons (Electronic Edition)*. Knovel, 2010.

[6] Carl L Yaws. *The Yaws handbook of vapor pressure: Antoine coefficients*. Gulf Professional Publishing, 2015.

[7] Carl L. Yaws. *Yaws' Critical Property Data for Chemical Engineers and Chemists*. Knovel, 2012; 2013; 2014.

[8] Hans W. Stock. Surface patterns on subliming and liquefying ablation materials. *AIAA Journal*, 13(9):1217–1223, 1975.

[9] A.L. Laganelli and D.E. Nestler. Surface ablation patterns: A phenomenology study. *AIAA Journal*, 7(7):1319–1325, 1969.

[10] C.O.White nd R.M. Grawbow. Crosshatch surface patterns-comparison of experiment with theory. *AIAA Journal*, 11(9):1316–1322, 1973.

[11] R.M.Grabow and C.O. White. A surface flow approach for predicting crosshatch patterns. *AIAA Journal*, 11(6):1316–1322, 1973.

[12] John B McDevitt. An exploratory study of the roll behavior of ablating cones. *Journal of Spacecraft and Rockets*, 8(2):161–169, 1971.

[13] Murray Tobak. Hypothesis for the origin of cross-hatching. *AIAA Journal*, 8.

[14] Harold Mirels. Origin of striations on ablative materials. *AIAA Journal*, 7(9):1813–1814, 1969.

[15] Hans W. Stock and Jean J. Ginoux. Experimental results on crosshatched ablation patterns. *AIAA Journal*, 9(5):971–973, 1971.

[16] Pu Qun. Cross-hatching-an interaction between shock and turbulent boundary layer. *Three-Dimensional Turbulent Boundary Layers;*, pages 254–264, 1982.

[17] Ronald F. Probstein Harris Gold and RObert S. Scullen. Inelastic deformation and crosshatching.

[18] Philip R. Nachtsheim and Howard K. Larson. Crosshatched ablation patterns in teflon. *AIAA Journal*, 9(8):1608–1614, 1971.

[19] R.L. Baker. Low temperature ablator nosetip shape change. *AIAA Paper*, (72-90), 1972.

[20] H.K.Larson and G.G Mateer. Cross-hatching - a coupling of gas dynamics with the ablation process. *AIAA Paper*, (68-670), 1968.

[21] E.P. Williams. Experimental studies of ablation surface patterns and resulting roll torques. *AIAA Journal*, 9(7):1315–1321, 1971.

[22] Max E. Wilkins Thomas N. Canning and Michael E. Tauber. Ablation patterns on cones having laminar and turbulent flows. *AIAA Journal*, 6(1):174–175, 1968.

[23] MR Wool. Interim report, passive nosetip technology (pant) program, volume x, summary of experimental and analytical results (for the period may 1973 to december 1974). *SAMSO, TR-74-86-Vol-X*, 1975.

[24] A.L. Laganelli and D.E. Nestler. Surface ablation patterns: A phenomenology study. *AIAA Journal*, 7(7):1319–1325, 1969.

[25] Thomas N Canning, ME Tauber, and ME Wilkins. Boundary-layer phenomena observed on the ablated surfaces of cones recovered after flights at speeds up to 7 km/sec. 1967.

[26] John B McDevitt. *Upwash patterns on ablating and nonablating cones at hypersonic speeds*. National Aeronautics and Space Administration, 1969.

[27] Eva M Winkler, Richard L Humphrey, Michael T Madden, and Joseph A Koeing. Substructure heating on cracked ablative heat shields. *AIAA Journal*, 8(10):1895–1896, 1970.

[28] AL Laganelli and RE Zempel. Observations of surface ablation patterns in subliming materials. *AIAA Journal*, 8(9):1709–1711, 1970.

[29] Rudolph J. Swigart. Cross-hatching studies-a critical review. *AIAA Journal*, 12(10):1301–1318, 1974.

[30] Philip R. Nachtsheim and Jack R. Hagen. Observations of crosshatched wave patterns in liquid films. *AIAA Journal*, 10(12):1637–1640, 1972.

[31] Philip R. Nachtsheim. Stability of crosshated wave patterns in thin liquid films adacent to supersonic streams. *Physics of Fluids*, 13(10):2432–2447, 1970.

[32] Ronald F. Probstein and Harris Gold. Cross-hatching: A material response phenomena. *AIAA Journal*, 8.

[33] Hans W. Stock and Jean J. Ginoux. Further experimental studies of cross-hatching. *AIAA Journal*, 10(4):557–558, 1972.

[34] CR Wilke. A viscosity equation for gas mixtures. *The journal of chemical physics*, 18(4):517–519, 1950.

[35] R Byron Bird, Warren E Stewart, and Edwin N Lightfoot. *Transport phenomena*, volume 1. John Wiley & Sons, 2006.

[36] Joseph O Hirschfelder, Charles F Curtiss, Robert Byron Bird, and Maria Goeppert Mayer. *Molecular theory of gases and liquids*, volume 165. Wiley New York, 1964.

[37] Frederick Gwynn Blottner, Margaret Johnson, and Molly Ellis. Chemically reacting viscous flow program for multi-component gas mixtures. Technical report, Sandia Labs., Albuquerque, N. Mex., 1971.

[38] Carl L Yaws. *Transport properties of chemicals and hydrocarbons*. William Andrew, 2014.

[39] JL Steger and RF Warming. Flux vector splitting of the inviscid equations with application to finite difference methods. 1979.

[40] Joseph L Steger and RF Warming. Flux vector splitting of the inviscid gasdynamic equations with application to finite-difference methods. *Journal of computational physics*, 40(2):263–293, 1981.

[41] R MacCormack. Current status of numerical solutions of the navier-stokes equations. In *23rd Aerospace Sciences Meeting*, page 32, 1985.

[42] Pramod K Subbareddy and Graham V Candler. A fully discrete, kinetic energy consistent finite-volume scheme for compressible flows. *Journal of Computational Physics*, 228(5):1347–1364, 2009.

[43] J Larsson, Ronan Vicquelin, and I Bermejo-Moreno. Large eddy simulations of the hyshot ii scramjet. *Center for Turbulence Research Annual Briefs*, pages 63–74, 2011.

[44] Travis William Drayna. *Design and Optimization of Hypersonic Inward-Turning Inlets*. University of Minnesota, 2011.

[45] Ioannis Nompelis, Travis Drayna, and Graham Candler. Development of a hybrid unstructured implicit solver for the simulation of reacting flows over complex geometries. In *34th AIAA Fluid Dynamics Conference and Exhibit*, page 2227, 2004.

[46] Ioannis Nompelis, Travis W Drayna, and Graham V Candler. A parallel unstructured implicit solver for hypersonic reacting flow simulation. In *Parallel Computational Fluid Dynamics 2005*, pages 389–395. Elsevier, 2006.

[47] Michael J Wright, Graham V Candler, and Deepak Bose. Data-parallel line relaxation method for the navier-stokes equations. *AIAA journal*, 36(9):1603–1609, 1998.

[48] Graham V. Candler Ioannis Nompelis and Raul J. Conti. A parallel implicit cfd code for the simultion of ablating re-entry vehicles.

[49] Vladimyr Gidzak and Graham Candler. Validation of fluid-structure interaction capabilities in us3d. In *21st AIAA Aerodynamic Decelerator Systems Technology Conference and Seminar*, page 2543, 2011.

[50] Loretta Trevino and Graham V Candler. Numerical simulation of regular surface patterns on sublimating ablative materials. In *53rd AIAA Aerospace Sciences Meeting*, page 1452, 2015.

[51] J.K Sherwood and C. Johannes. The maximum rate of sublimation of solids. *A.I.Ch. E. Journal*, 8(5):590–593, 1962.

[52] Charles David Hodgman, Max Frankel, et al. Handbook of chemistry and physics. 1960.

[53] WE Welsh Jr. Shape and surface roughness effects on turbulent nosetip ablation. *AIAA Journal*, 8(11):1983–1989, 1970.

[54] Derek J Dinzl and Graham V Candler. Direct simulation of hypersonic crossflow instability on an elliptic cone. *AIAA journal*, 55(6):1769–1782, 2017.

[55] Joel Gronvall, Heath Johnson, and Graham Candler. Hypersonic three-dimensional boundary layer transition on a cone at angle of attack. In *42nd AIAA Fluid Dynamics Conference and Exhibit*, page 2822, 2011.

[56] P.R.Spalart. Topics in industrial viscous flow calculation. In *Invited Lecture, Colloquium:Transitional Boundary Layers in Aeronautics, Royal Netherlands Academy of Ats and Sciences*, 1995.

[57] SA Gaponov and BV Smorodsky. Laminar supersonic boundary layer of binary gas mixture. *Vestnik NSU. Series: Physics*, 11(1):5–15, 2016.

[58] Sergey A Gaponov and Boris V Smorodsky. On stability of the supersonic boundary layer with a foreign gas injection. In *AIP Conference Proceedings*, volume 1770, page 030047. AIP Publishing LLC, 2016.

[59] Sergey A Gaponov and Boris V Smorodsky. Supersonic boundary layer of binary mixture and its stability. *International Journal of Mechanics*, 10:312–319, 2016.

Appendix A

Temporal Progression of Flat Plate Simulations

A.1 Baseline Reynolds Number

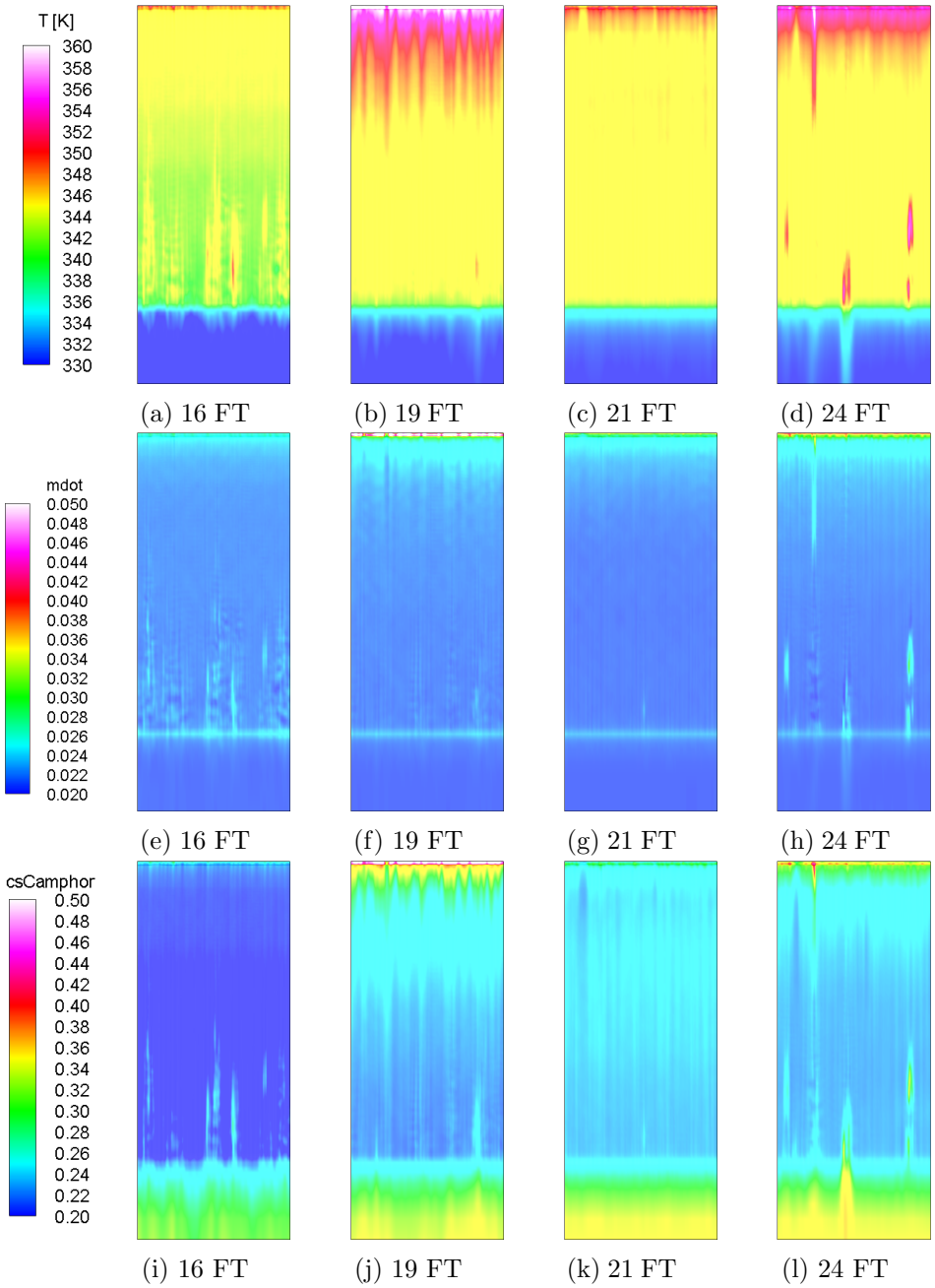

(a) 16 FT (b) 19 FT (c) 21 FT (d) 24 FT

(e) 16 FT (f) 19 FT (g) 21 FT (h) 24 FT

(i) 16 FT (j) 19 FT (k) 21 FT (l) 24 FT

Figure A.1: Flow Time (FT) Progression of Wall Temperature (top row), Camphor Mass Flux (middle row), and Camphor Mass Fraction (bottom row).

A.2 Low Reynolds Number

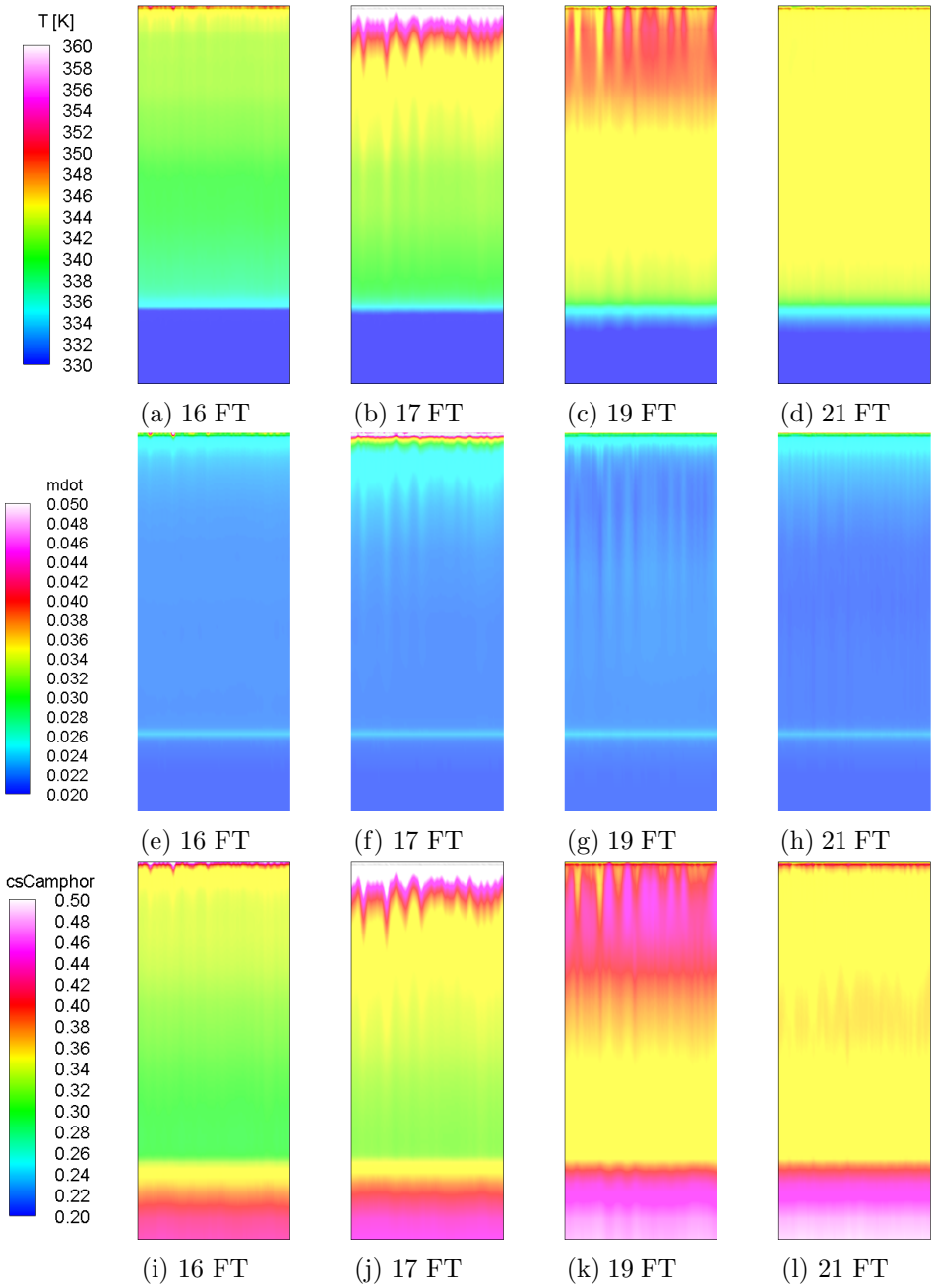

(a) 16 FT (b) 17 FT (c) 19 FT (d) 21 FT

(e) 16 FT (f) 17 FT (g) 19 FT (h) 21 FT

(i) 16 FT (j) 17 FT (k) 19 FT (l) 21 FT

Figure A.2: Flow Time (FT) Progression of Wall Temperature (top row), Camphor Mass Flux (middle row), and Camphor Mass Fraction (bottom row).

A.3 High Reynolds Number

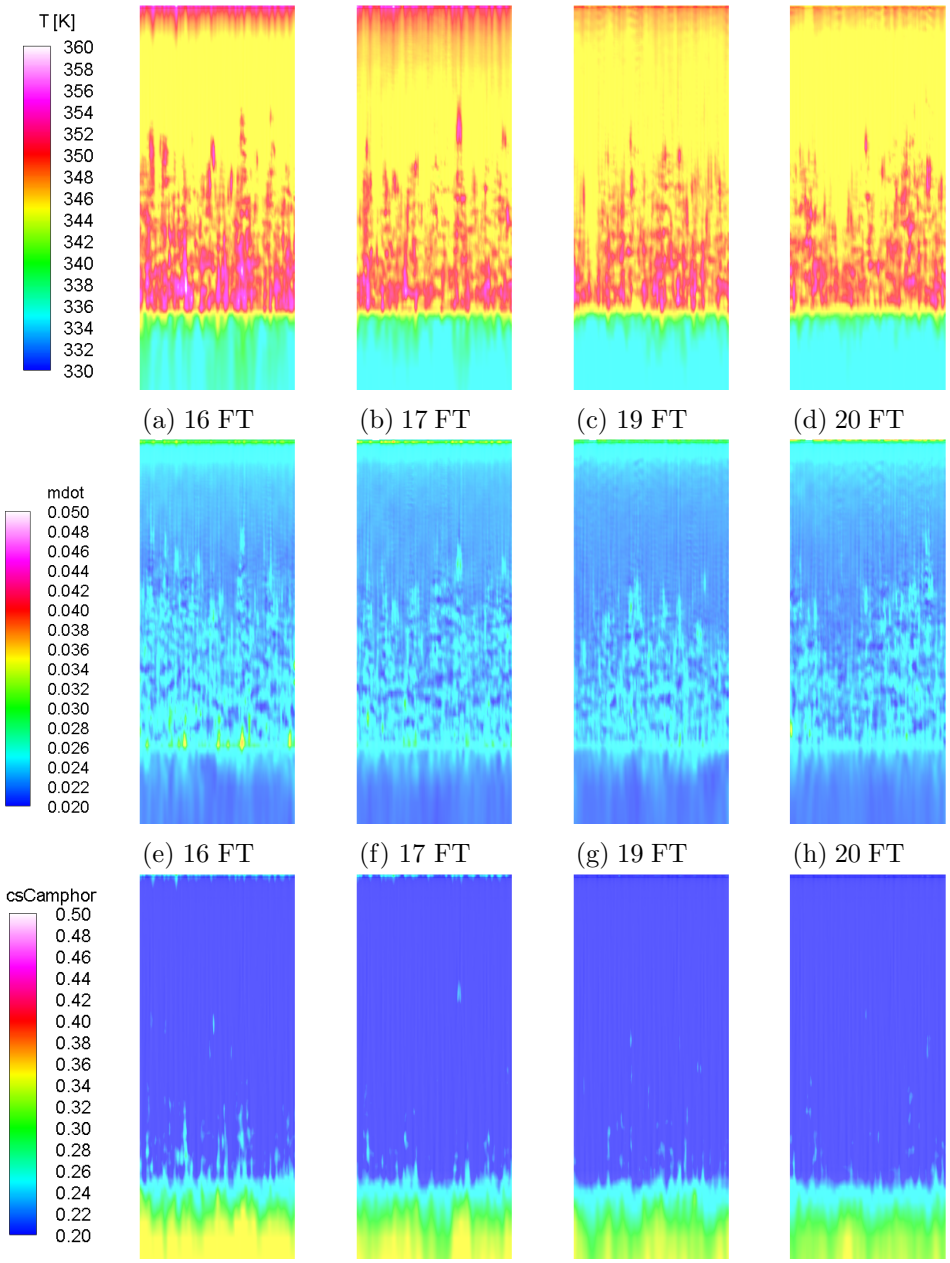

(a) 16 FT (b) 17 FT (c) 19 FT (d) 20 FT

(e) 16 FT (f) 17 FT (g) 19 FT (h) 20 FT

(i) 16 FT (j) 17 FT (k) 19 FT (l) 20 FT

Figure A.3: Flow Time (FT) Progression of Wall Temperature (top row), Camphor Mass Flux (middle row), and Camphor Mass Fraction (bottom row).

A.4 Baseline Reynolds Number No Shape Change

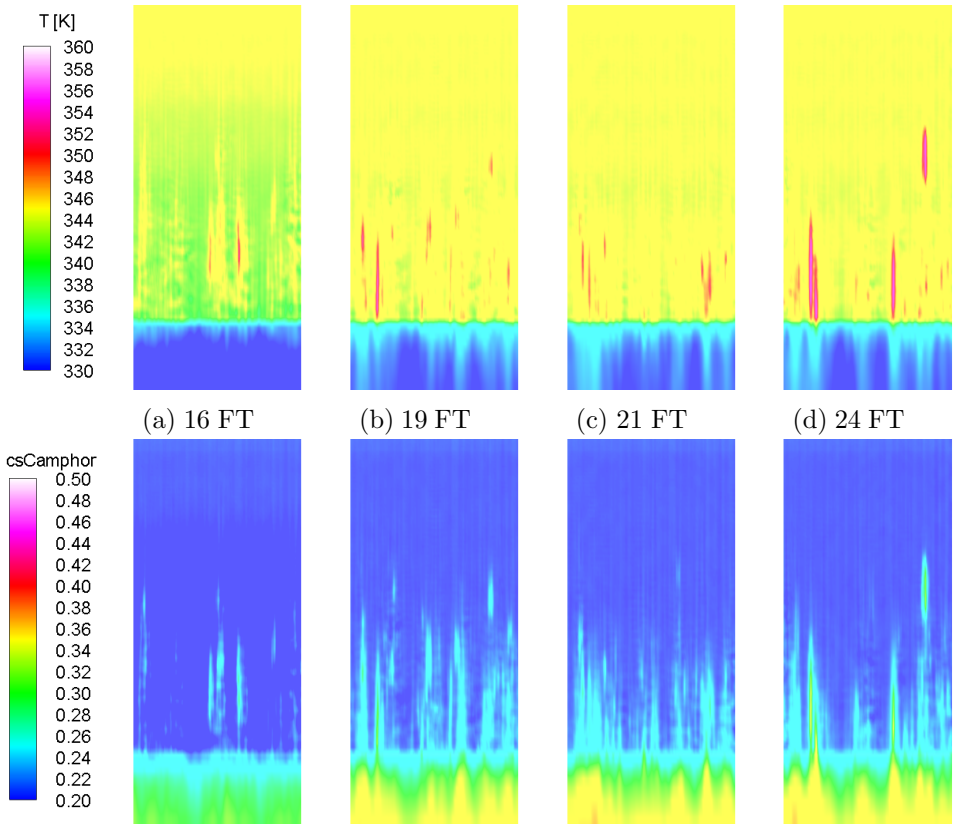

(a) 16 FT (b) 19 FT (c) 21 FT (d) 24 FT

(e) 16 FT (f) 19 FT (g) 21 FT (h) 24 FT

Figure A.4: Flow Time (FT) Progression of Wall Temperature (top row) and Camphor Mass Fraction (bottom row).

Appendix B

Supplemental CFD Simulation

B.1 Flat Plate with Numerical Trips

Simulations were performed through the exploratory process of validating the ablation boundary condition and analyzing the flows for which crosshatching was observed. The objective of this simulation was a proof of concept and to illustrate that turbulent wedges can mimic crosshatching-like patterns. The freestream conditions are the laminar Baker conditions performed in the validation study.

Four equally spaced numerical trips were placed at the steel-camphor junction. The temporal progression of shape change is illustrated in Figure B.1. Initially, the surface is smooth, and as the simulation progresses, the divots start to form downstream of the trip location. Eventually, the turbulent wedges start to interact, and diamond shape patterns begin to form. The pattern length scales were effectively forced due to the placement of the trips and did not match with the wavelengths or angles observed in experiments. It is unlikely that turbulent wedges, modeling in this form are the mechanism for crosshatching.

Mach	To	Po	AoA
–	[K]	[MPa]	[deg]
5.00	797	0.8	10

Table B.1: Baker Laminar Tunnel Conditions for Flat Plate Simulation

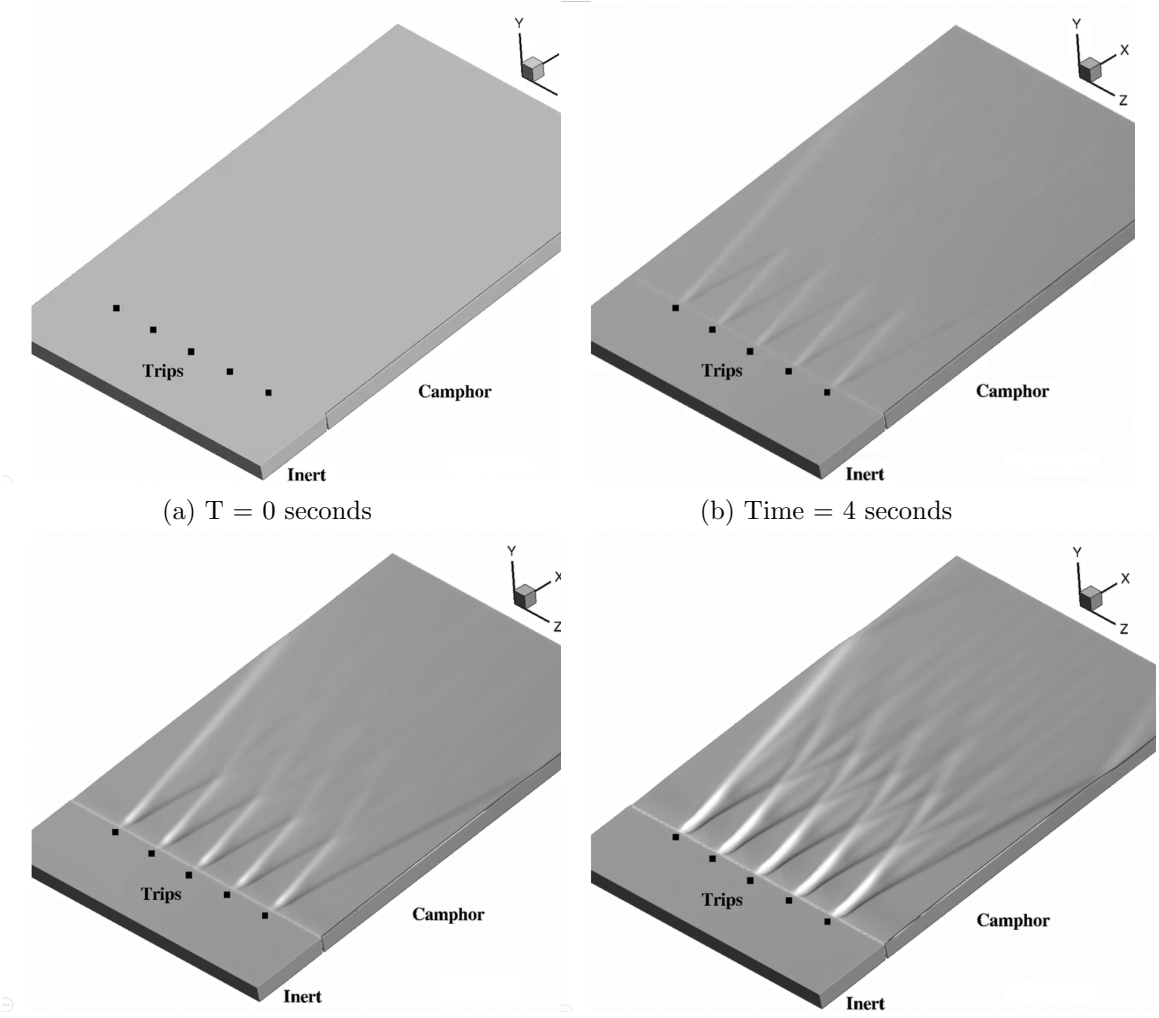

(a) T = 0 seconds

(b) Time = 4 seconds

(c) Time = 12 seconds

(d) Time = 16 seconds

Figure B.1: Temporal Progression of Shape Change

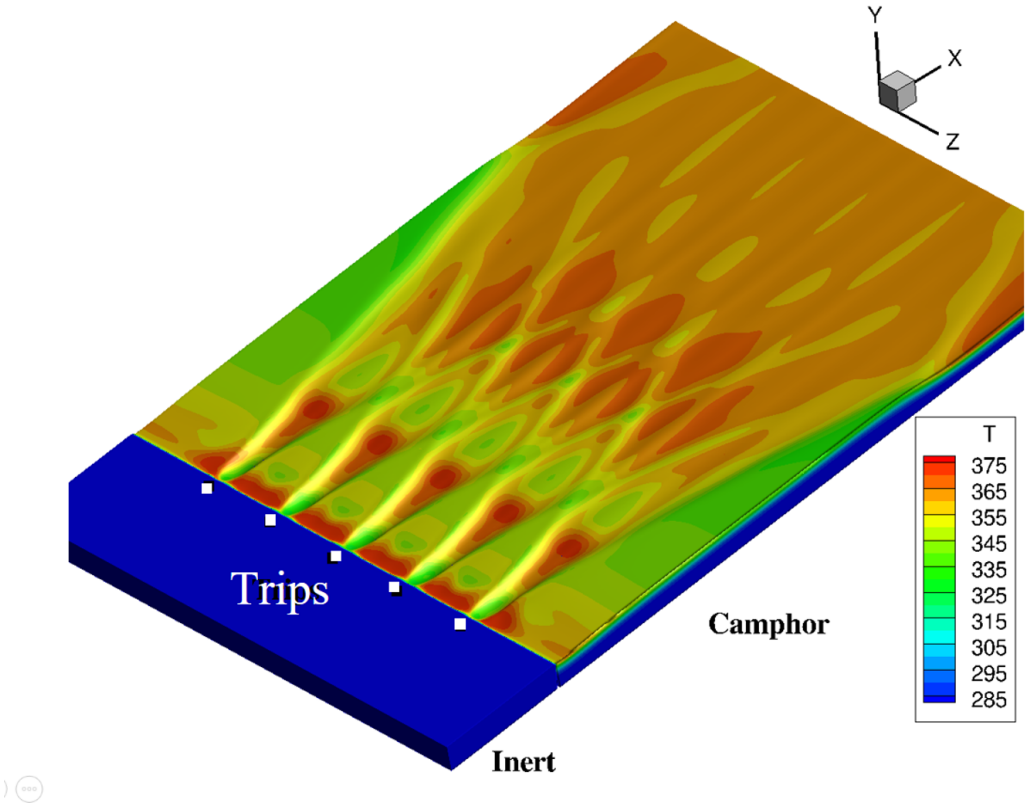

Figure B.2: Temperature Contours at Time = 16 seconds

Appendix C

Thermodynamic, Transport and Physical Properties of Camphor

Table C.1: Camphor Properties [2]

Property	Camphor (d-)
Formula	$C_{10}H_{16}O$
Molecular Weight	152.23
Crystalline form	hexagonal
Density (solid) (gr/ml)	0.99
Enthalpy of sublimation (cal/gr)	58.5
Thermal conductivity (solid) (cal/cm sec ^{o} C)	0.96×10^{-3}

Table C.2: Enthalpy of Formation Camphor Gas [3]

Formula	$H_f = A+BT+CT^2+DT^3+ET^4$
Range(K)	T_{min}=150,T_{max}=1500
A	-200.216
B	-0.23535
C	1.504E-04
D	5.448E-09

E	-1.641E-11

Table C.3: Heat Capacity of Camphor Gas [4]

Formula	Cp_{gas} = A+BT+CT^2+DT^3+ET^4+FT^5+GT^6
Range(K)	T_{min}=150,T_{max}=1500
A	253.4458281
B	-2.292259271
C	0.011512294
D	-2.11364E-05
E	1.95203E-08
F	-9.02255E-12
G	1.65636E-15

Table C.4: Heat Capacity of Camphor Solid [4]

Formula	Cp_{solid} = A+BT+CT^2
Range(K)	T_{min}=293,T_{max}=328
A	230.05
B	0.13811
C	0.00

Table C.5: Camphor Diffusion Coefficient in Air[5]

Formula	D_{12} = A+BT+CT^2
Range(K)	T_{min}=200,T_{max}=1500
A	-0.0815723
B	0.000407754
C	2.52604E-07

Table C.6: Camphor Gas Viscosity [5]

Formula	μ = A+BT+CT^2+DT^3
Range(K)	T$_{min}$=250,T$_{max}$=1500
A	-0.743912
B	0.202152
C	1.21454E-05
D	-1.56199E-08

Table C.7: Camphor Gas Thermal Conductivity [5]

Formula	κ = A+BT+CT^2+DT^3
Range(K)	T$_{min}$=250,T$_{max}$=1500
A	-0.00438282
B	1.04999E-05
C	1.32595E-07
D	-4.94992E-11

Table C.8: Camphor Gas Vapor Pressure [6]

Formula	log P = A-B/(T+C) (mm Hg)
Range(^{0}C)	T$_{min}$=-15.80,T$_{max}$=435.85
A	6.95669315563984
B	1650.62714530972
C	197.554464934728
D	-4.94992E-11

Table C.9: Enthalpy of Camphor Gas [7]

Formula	ΔH= A+BT+CT^2+DT^3+ET^4
Range(K)	T$_{min}$=150,T$_{max}$=1500
A	-20.625998

B	-0.054510
C	4.53799E-04
D	-1.33750046E-07
E	1.0557666E-11